Unsteady interaction mechanism of transverse stage separation in hypersonic flow for a two-stage-to-orbit vehicle ⊘

Wang Yue (王粤) ; Wang Yunpeng (汪运鹏) ✉ ; Jiang Zonglin (姜宗林)
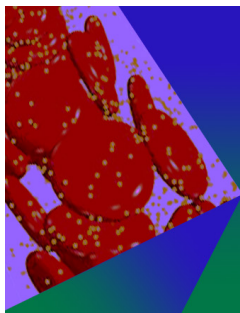
Check for updates

CrossMark

View Online

Export Citation

Physics of Fluids

Special Topic: Flow and Forensics

Submit Today!

AIP Publishing

AIP Publishing

Unsteady interaction mechanism of transverse stage separation in hypersonic flow for a two-stage-to-orbit vehicle

View Online   Export Citation   CrossMark

Yue Wang (王粤),[1,2] (iD) Yunpeng Wang (汪运鹏),[1,2,a] (iD) and Zonglin Jiang (姜宗林)[1,2] (iD)

AFFILIATIONS

[1]State Key Laboratory of High-Temperature Gas Dynamics, Institute of Mechanics, Chinese Academy of Sciences, Beijing 100190, China
[2]School of Engineering Sciences, University of Chinese Academy of Sciences, Beijing 100049, China

Note: This paper is part of the special topic, Hypersonic Flow.
[a]Author to whom correspondence should be addressed: wangyunpeng@imech.ac.cn

ABSTRACT

Due to the complex aerodynamic interaction, the safe separation of two stages is one of the challenges for the successful launch of a two-stage-to-orbit (TSTO) vehicle. The unsteady hypersonic flow past the parallel-staged TSTO model during stage separation at $Ma = 6.7$ and $Re = 8.86 \times 10^5$ m^{-1} is numerically studied using laminar flow simulation. The TSTO model consisted of a waverider and a spaceplane as booster and orbiter, respectively. The effect of the center of gravity (CoG) of the orbiter on the unsteady aerodynamic interference during stage separation of TSTO is analyzed in detail with $0.65 \le l_{\mathrm{CoG}}/l_{\mathrm{o}} \le 0.80$. In addition, the aerodynamic characteristics, dynamic behaviors, and unsteady wall pressure variation are compared in different cases. The results show that the CoG regime is limited to 5% of the orbiter length for absolutely safe separation, i.e., $0.70 < l_{\mathrm{CoG}}/l_{\mathrm{o}} < 0.75$. As for the unsuccessful separation, the orbiter tends to fly nose-down if $l_{\mathrm{CoG}}/l_{\mathrm{o}} \le 0.70$ while tending to pitch or somersault when $l_{\mathrm{CoG}}/l_{\mathrm{o}} = 0.80$. Furthermore, the pitching moment of the orbiter, which is influenced by the interstage shock wave–boundary layer interaction and shock–shock interaction, dominates the separation safety, and the specific flow mechanisms concerning the separation behavior associated with aerodynamic interference in different cases are analyzed in detail.

Published under an exclusive license by AIP Publishing. https://doi.org/10.1063/5.0151663

I. INTRODUCTION

The parallel-arrangement two-stage-to-orbit (TSTO) reusable launch vehicle is expected to realize the dream of traveling around the world in one hour at a low cost, and it has attracted extensive research attention.[1,2] Apart from hypersonic air-breathing propulsion technology,[3] safe stage separation is also a fundamental challenge for TSTO, which directly determines the success of the mission. In addition, the supersonic and hypersonic flow past a multi-body system is inherently complex and difficult to eliminate due to strong shock–shock interaction (SSI), shock–boundary layer interaction (SBLI), etc.[4–16] The parallel TSTO vehicle usually consists of the booster with a combined air-breathing engine and the orbiter with a rocket engine,[3] and the stage separation typically happens in the hypersonic regime, i.e., Mach 6–7. Unsteady hypersonic flow with strong and complex aerodynamic interference for multi-body motion complicates the stage separation for TSTO.

The separation scheme affects the separation behavior of the two stages and is related to the safety of vehicle.[17] With the conventional scheme, i.e., transverse stage separation (TSS), the orbiter detaches along the direction perpendicular to the booster with a noticeable variation gap, resulting in strong aerodynamic interference between the stages. Wang *et al.*[17–19] proposed a new separation scheme, i.e., longitudinal stage separation. Specifically, the orbiter moves along the upper surface of the booster with small or zero gaps to avoid strong aerodynamic interference and achieve safer separation. The feasibility of longitudinal stage separation was verified by the dynamic test in the JF-12 duplicate flight condition shock tunnel. This is the first dynamic active separation test for the parallel-arranged TSTO vehicle in the shock tunnel.[20,21] The complex flow mechanism associated with strong aerodynamic interference during TSTO stage separation has been a hot research topic. In the 1960s, Decker[22] conducted a wind tunnel study to investigate the aerodynamic interference associated

with simple parallel-staged TSTO configurations at Mach 3 and 6. In addition, Decker and Wilhite[23] summarized the effects of various parameters on the separation maneuver from the Space Shuttle configurations. Schroder and Hartmann[24] performed an inviscid and viscous simulation for perfect and equilibrium Mach 6 hypersonic real gas flows over the Saenger TSTO vehicle. The simulation results showed good agreement with the experimentally measured aerodynamics, and it was found that the influence of the orbiter on the flow over the booster weakened with increasing angle of incidence. The perfect gas assumption was validated. Cvrlje et al.[25] performed the unsteady flow simulation for TSTO, where the orbiter performs yaw and roll oscillations with defined frequencies over the booster at a certain distance, and analyzed the flowfields and wall pressure as well as the aerodynamics. The results indicated that the unsteadiness during the separation could not be neglected. At NASA, Bordelon et al.[26] performed stage separation wind tunnel tests on the LGBB (Langley Glide-Back Booster) TSTO vehicle to determine the aerodynamic forces and moments of interference and to analyze the flowfields between the stages. They found that the aerodynamics are dominated by complex SSI, which causes the booster to be statically unstable at several separation positions. Murphy et al.[27] developed experimental tools and test methods to solve the stage separation problems for the LGBB TSTO vehicle based on the aerodynamic database from the benchmark wind tunnel test. The results of the test program showed excellent agreement with both inviscid and viscous computational predictions and experimental results. Ozawa et al.[28,29] investigated the aerodynamic interactions of a simple two-dimensional TSTO model at Mach 8.1 in a shock tunnel. The flow pattern was classified according to the interstage clearance and SSI pattern, and the flow mechanism of a feedback loop related to shock oscillations was analyzed. Wang et al.[30] performed the computational fluid dynamics (CFD) analysis of the flow characteristics and physical mechanism of the stage separation for double wedge TSTO configurations and investigated the effect of incidence angle on the stage separation in depth. The results showed that the intensity of interference upgrades as the incidence angle increases, while it degrades as the interstage gap increases. Moreover, the incidence angle between 6° and 8° may be conducive to the safe separation for the TSTO model. Lin et al.[31] developed a two-body synchronous captive trajectory system (CTS) test technique and applied it in the hypersonic wind tunnel to acquire the separation trajectory and aerodynamic characteristics of the TSTO model.

The finished research works on the transverse stage separation for the parallel-staged two-body configurations studied the interstage interference and associated aerodynamics at high speeds, and compared and validated the results between CFD and wind tunnel tests. These works have shown that aerodynamic interference involves strong shock waves and the viscous boundary layer plays a role in stage separation, and especially the resulting unsteadiness and vehicle instability in the stage separation needs to be carefully treated, despite some results being carried out in the static stage separation and quasi-steady way. Moreover, the study of the static or quasi-steady stage separation have limitations when it comes to capturing the unsteady and highly coupling effects of the strong aerodynamic interference and the multibody motion in hypersonic flow. Furthermore, the flow mechanism and separation characteristics of the parallel-staged complex TSTO configuration should be understood in depth, though the flowfields of

dynamic stage separation have been studied extensively with the simple TSTO configuration. On the other hand, the effects of a few critical parameters on TSTO stage separation were examined in detail, such as interstage incidence angle, gaps, and so on. However, the effect of the vehicle's center of gravity (CoG) on stage separation has not been investigated yet. To bridge this research gap, in this paper, the effect of the orbiter's CoG on stage separation is numerically investigated for a TSTO vehicle with complex geometry and parallel stages. The flow patterns, interaction structure, and strong aerodynamic interference coupled with the orbiter's separation behavior are analyzed in detail. Moreover, the flow mechanism associated with the aerodynamics of the vehicle is revealed. The variation range of the orbiter's CoG for the safe separation of the TSTO vehicle is also clarified.

II. COMPUTATIONAL TSTO MODEL

The TSTO configuration for the stage separation study in this research consists of a waverider and a spaceplane as the booster and orbiter, respectively. More detailed information on the TSTO vehicle can be found in Ref. 19. Figure 1 shows a schematic illustration of the size of the TSTO computational model. In addition, the leading edge of both vehicles models is blunted with a blunt radius of 1 mm. The length of the booster is $l_b = 1$ m, and its CoG is located at 0.738, -0.05, and 0 m. The length of the orbiter is $l_o = 0.4$ m, and its CoG is the only independent variable ($l_{CoG}/l_o = 0.65, 0.675, 0.687, 0.70, 0.705, 0.71, 0.725, 0.75, 0.80$). In addition, the perpendicular offset of the CoG of the orbiter to the lower surface is $h_{CoG}/d_o = 0.32$. The initial minimum interstage clearance is $h/l_b = 0.015$, and the initial incidence angle of the orbiter is 8°. In addition, the AoA of the freestream is zero. The non-dimensional mass of the orbiter is $m_o/\rho_\infty l_o^3 = 2660$, and the moments of inertia are $I_{xx}/\rho_\infty \cdot l_o^5 = 18$, $I_{yy}/\rho_\infty \cdot l_o^5 = 165$, and $I_{zz}/\rho_\infty \cdot l_o^5 = 154$, respectively. The density of the freestream is $\rho_\infty = 0.0074$ kg·m^{-3}. The moment of inertia of the orbiter is assumed to be invariant in different cases for the numerical simulation due to the small offset of the CoG and the small mass of the orbiter so that
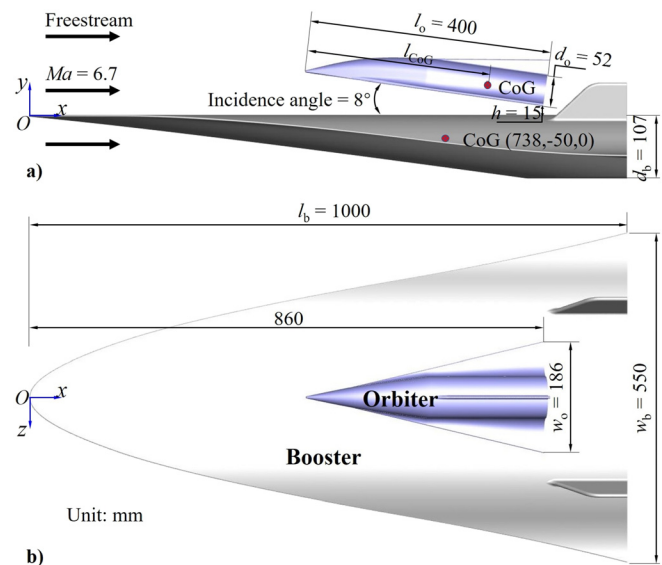
FIG. 1. The schematic illustration of the overall size of the TSTO configuration.

the variation of the moment of inertia can be ignored. Furthermore, for the dynamic stage separation simulation, the booster is assumed to be stationary, while the orbiter detaches freely from the initial position shown in Fig. 1 and is subjected to six-degree-of-freedom (6-DOF) motion equations under the flow forces, moments, and gravity. The moment reference point is located at the CoG. Additionally, the attachments and mechanical structures between the stages, as well as engines, are not considered in the numerical simulation, and their effects on the stage separation are not analyzed in this paper.

III. COMPUTATIONAL METHODS AND VALIDATIONS
A. Governing equations and numerical methods

The unsteady three-dimensional (3D) Navier–Stokes (N–S) equations employed for the simulation of dynamic TSS of the TSTO are given by

$$\frac{\partial}{\partial t}\iiint_{\Omega} \boldsymbol{W} d\Omega + \oiint_{\partial\Omega}(\boldsymbol{F_c} - \boldsymbol{F_v})d\boldsymbol{S} = 0, \tag{1}$$

where $\boldsymbol{W}$, $\boldsymbol{F_c}$, and $\boldsymbol{F_v}$ are the vectors of conservative variables, convective fluxes, and viscous fluxes, respectively, which are expressed as

$$\boldsymbol{W} = \begin{pmatrix} \rho \\ \rho u \\ \rho v \\ \rho w \\ \rho E \end{pmatrix}, \quad \boldsymbol{F_c} = \begin{pmatrix} \rho V_r \\ \rho u V_r + n_x p \\ \rho v V_r + n_y p \\ \rho w V_r + n_z p \\ \rho H V_r + V_g p \end{pmatrix},$$

$$\boldsymbol{F_v} = \begin{pmatrix} 0 \\ n_x\tau_{xx} + n_y\tau_{xy} + n_z\tau_{xz} \\ n_x\tau_{yx} + n_y\tau_{yy} + n_z\tau_{yz} \\ n_x\tau_{zx} + n_y\tau_{zy} + n_z\tau_{zz} \\ n_x\Theta_x + n_y\Theta_y + n_z\Theta_z \end{pmatrix}, \tag{2}$$

where ρ is the density; u, v, and w are the velocity components in the x, y, and z directions; p is the pressure and $p = (\gamma - 1)[\rho E - 1/2\rho(u^2 + v^2 + w^2)]$ (γ is the specific heat ratio); E and H are the total energy and total enthalpy per unit mass, and $H = E + p/\rho$; τ_{ij} is the component of viscous stress; Θ_x, Θ_y, and Θ_z are the heat conduction; n_x, n_y, and n_z are the components of outward-facing unit normal vector; V_r represents the contravariant velocity relative to the motion of the grid, which is expressed as

$$\boldsymbol{V_r} = \boldsymbol{V} - \boldsymbol{V_g} = (u - u_g)n_x + (v - v_g)n_y + (w - w_g)n_z, \tag{3}$$

where $\boldsymbol{V_g} = u_g n_x + v_g n_y + w_g n_z$ is the contravariant velocity at the surface of the control volume. To close the system of equations, the ideal gas equation of state is introduced: $p = \rho RT$. Additionally,

$$\Theta_x = u\tau_{xx} + v\tau_{xy} + w\tau_{xz} + k_T\frac{\partial T}{\partial x}, \tag{4}$$

$$\Theta_y = u\tau_{yx} + v\tau_{yy} + w\tau_{yz} + k_T\frac{\partial T}{\partial y}, \tag{5}$$

$$\Theta_z = u\tau_{zx} + v\tau_{zy} + w\tau_{zz} + k_T\frac{\partial T}{\partial z}, \tag{6}$$

where k_T is the coefficient of thermal conductivity and T is the temperature. The components of the viscous stress tensor are obtained from the following relations:

$$\tau_{xx} = 2\mu\frac{\partial u}{\partial x} - \frac{2}{3}\mu\left(\frac{\partial u}{\partial x} + \frac{\partial v}{\partial y} + \frac{\partial w}{\partial z}\right), \tag{7}$$

$$\tau_{yy} = 2\mu\frac{\partial v}{\partial y} - \frac{2}{3}\mu\left(\frac{\partial u}{\partial x} + \frac{\partial v}{\partial y} + \frac{\partial w}{\partial z}\right), \tag{8}$$

$$\tau_{zz} = 2\mu\frac{\partial w}{\partial z} - \frac{2}{3}\mu\left(\frac{\partial u}{\partial x} + \frac{\partial v}{\partial y} + \frac{\partial w}{\partial z}\right), \tag{9}$$

$$\tau_{xy} = \tau_{yx} = \mu\left(\frac{\partial u}{\partial y} + \frac{\partial v}{\partial x}\right), \tag{10}$$

$$\tau_{xz} = \tau_{zx} = \mu\left(\frac{\partial u}{\partial z} + \frac{\partial w}{\partial x}\right), \tag{11}$$

$$\tau_{yz} = \tau_{zy} = \mu\left(\frac{\partial w}{\partial y} + \frac{\partial v}{\partial z}\right), \tag{12}$$

where μ is the viscosity coefficient.

The N–S equations are solved with the cell-vertex finite volume method for spatial discretization.[32] The inviscid flux is computed with a second-order upwind scheme using the Harten-Lax-van Leer contact (HLLC) approximate Riemann solver.[33] The spatial variables are interpreted by second-order total variation diminishing (TVD) polynomial interpolation with a minmod limiter for stability.[34] The viscous flux is computed by a simple second-order average of all vertex polynomials. The viscosity coefficient is evaluated based on Sutherland's law.[35] The time advancement is performed by the backward Euler method integrated with multigrid acceleration and dual time-stepping method.[36] To obtain time-accurate unsteady results, the non-dimensional computational time step is $dt \cdot U_\infty/l_b = 0.1282$, where dt is the dimensional time step and $U_\infty = 2564\,\mathrm{m \cdot s^{-1}}$ is the freestream speed. The freestream conditions are $Ma_\infty = 6.7$, $Re_\infty = 8.86 \times 10^5\,\mathrm{m^{-1}}$, $q_\infty = 24217\,\mathrm{Pa}$, $p_\infty = 773\,\mathrm{Pa}$, $T_\infty = 365\,\mathrm{K}$, $p_0 = 3.95\,\mathrm{MPa}$, $T_0 = 3108\,\mathrm{K}$, and $H_0 = 3.65\,\mathrm{MJ \cdot kg^{-1}}$, which is a typical test flow condition of JF-12 duplicate flight conditions shock tunnel. Although the rarefied gas effects and nonequilibrium real gas effects usually become key issues at the sceneries of very hypervelocity and high-enthalpy flow conditions,[37,38] such as hypersonic flows associated with spacecraft reentry into the upper atmosphere,[39] the hypersonic flow investigated is still the continuous flow and the laws of N–S equations are still applicable since the Knudsen number is sufficiently small (around 1.2×10^{-5}) and less than 0.05. Moreover, the freestream gas property is a calorically perfect gas, and the real gas effect is not considered in the work, because the real gas effect does not play a role in such enthalpy airflow conditions, and it would be notable at higher enthalpy conditions, such as $H_0 > 5\,\mathrm{MJ \cdot kg^{-1}}$. Thus, it is appropriate to consider the perfect gas and to neglect real gas effects in the flow problems considered, and the reliability of the perfect gas N–S equations simulation is also proved in the validations even though the higher enthalpy is considered. As for the boundary conditions, the non-slip adiabatic wall condition is adopted for the wall, the freestream condition is adopted for the inflow, and the supersonic outflow condition is adopted, under which the boundary state from the interior flowfield is extrapolated. Moreover, laminar flow is assumed for the simulation since the flow did not transition to the turbulent

flow with $l_b = 1$ m at such a small inflow Reynolds number, which has been validated by experiments of the laminar boundary layer on a large-scale flat plate conducted in JF-12 shock tunnel at similar test flow condition.[40] Furthermore, previous studies have shown that numerical simulation results for laminar flow of the TSTO model agree well with wind tunnel test results and computed results for turbulent flow; therefore, the flow over the TSTO can be assumed laminar depending on the flow parameters.[41,42]

The 6-DOF rigid body dynamic (RBD) motion is governed by

$$m\left(\frac{dV_x}{dt} - V_y\omega_z + V_z\omega_y\right) = F_x, \tag{13}$$

$$m\left(\frac{dV_y}{dt} - V_z\omega_x + V_x\omega_y\right) = F_y, \tag{14}$$

$$m\left(\frac{dV_z}{dt} - V_x\omega_y + V_y\omega_x\right) = F_z, \tag{15}$$

$$I_{xx}\frac{d\omega_x}{dt} - (I_{yy} - I_{zz})\omega_y\omega_z = M_x, \tag{16}$$

$$I_{yy}\frac{d\omega_y}{dt} - (I_{zz} - I_{xx})\omega_z\omega_x = M_y, \tag{17}$$

$$I_{zz}\frac{d\omega_z}{dt} - (I_{xx} - I_{yy})\omega_x\omega_y = M_z. \tag{18}$$

Equations (13)–(15) represent the translation of the CoG of the body and Eqs. (16) and (17) represents the rotation of the CoG in the body's axial system. Here, m is the mass of the body; V_x, V_y, and V_z are the velocity components of the body (also the velocity of the orbiter grid, V_g); ω_x, ω_y, and ω_z are the components of the angular velocity of the body; F_x, F_y, and F_z are the components of applied force on the body, including aerodynamic forces and gravity; I_{xx}, I_{yy}, and I_{zz}

are the principal moments of inertia of the body; M_x, M_y, and M_z are the components of the applied moment on the body.

In the coupling of the flow solver and 6-DOF RBD dynamics solver for the stage separation of the TSTO, the forces and moments are computed from the flow solver as the input of the 6-DOF solver, and then, the linear and angular displacements of the orbiter can be updated by numerically integrating the 6-DOF equations with fourth-order Runge–Kutta method. Based on the displacements, the relative position of the two stages and the overset grid are updated. This iterative process is repeated until the end of the computation.

B. Computational grid and grid independency study

Considering the advantages of the overset grid methodology in solving the multi-body relative motion problem, it is adopted to simulate the dynamic separation of the TSTO vehicle. Figure 2 presents the overset grid and sketch of the boundary conditions in the numerical study. As shown in Fig. 2(a), the computational grid consists of two sub-grids, i.e., orbiter grid and booster grid. Both grids are generated by the hybrid meshing method and are composed of unstructured and structured blocks, including hexahedral, tetrahedral, pyramid, and triangular prism cell types. The first cell spacing normal to the wall is chosen to ensure $y^+ \sim 1$, and a progression ratio of 1.1 is applied to cluster the grid points radially outward from the wall and 40 cells spanning the thickness of the boundary layer to accurately capture the boundary layer flow physics.

The overset method applied for dynamic simulation involves the connection of the two sub-grids by hole cutting and data interpolation at every time step, as shown in Figs. 2(b) and 2(c). The outer boundary of the orbiter grid is defined as the cutter boundary, and accordingly, the cells from the booster grid that intersect with the cutter boundary
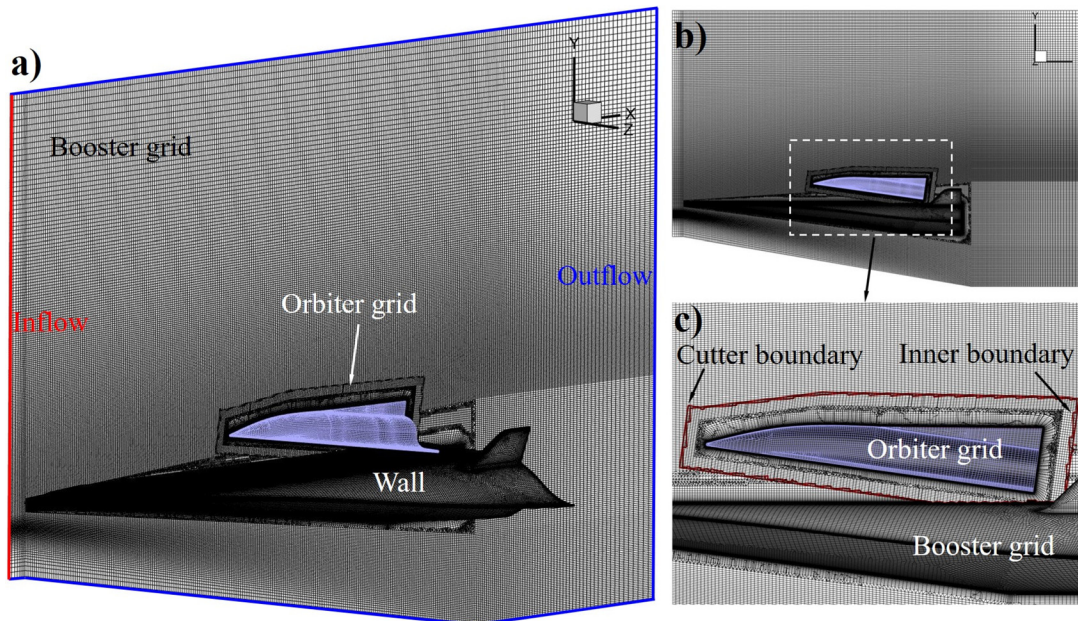

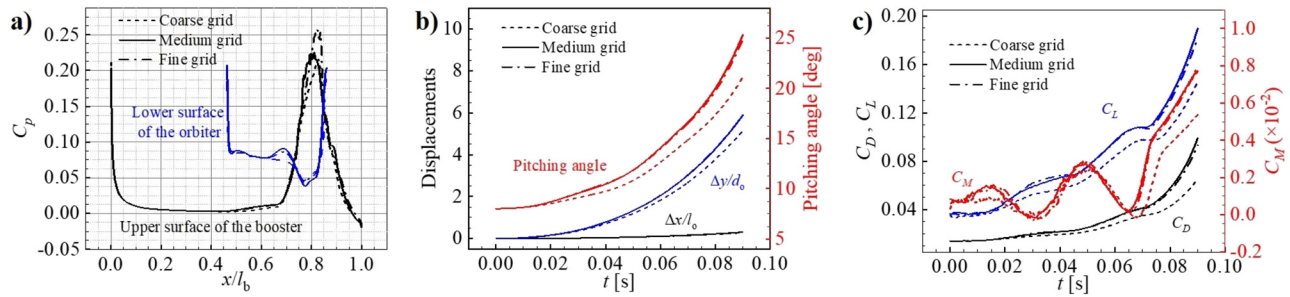**FIG. 2.** The schematic of the computational overset grid in the study.

FIG. 3. Grid independency study: (a) pressure coefficient along the surface of the vehicle, (b) the separation motion of the orbiter, and (c) aerodynamic coefficients of the orbiter in the $l_{CoG}/l_o = 0.71$ case in three computational grids.

are identified as the cutter cells. Then, the cells from the booster grid within the orbiter grid are cut off, creating the inner boundary of the booster grid. The cutter boundary and inner boundary enclose the overset cells of the two sub-grids. Afterward, the flow date is exchanged and interpolated on the overset cells to achieve second-order accuracy within two or more layers of interpolated grid points. More details of the overset grid can be found in related studies.[43] In the separation of TSTO, the sub-girds remain unchanged, but the overset grid is updated with the movement of the orbiter at every time step. The flow data are exchanged between the grid, and the computation of the entire flowfield is completed.

In the current study, three grids generated by the same approach but with varying resolutions are used to verify the grid independency. The three grids are coarse grid, medium grid, and fine grid, with approximately 8×10^6, 17×10^6, and 35×10^6 cells, respectively. Figure 3(a) displays the pressure coefficients of the symmetry lines on the upper surface of the booster and lower surface of the orbiter computed from the three grids before separation. Figures 3(b) and 3(c) show the displacements, pitching angle, and aerodynamic coefficients of the orbiter computed from the three grids during separation in the case with $l_{CoG}/l_o = 0.71$. All curves of the three grids display approximately the same variation tendency. Moreover, the values computed from the medium and fine grids are closer at the feature points. Therefore, the medium grid is selected for subsequent analysis.

C. Computational time step independency study

In the current study, the computation of the three different time steps with the same medium grid are used to verify the time step independency. The non-dimensional time step is set as $dt \cdot U_\infty / l_b = 0.256\,4$, $0.128\,2$, $0.051\,28$, respectively. Figure 4 presents the displacements, pitching angle, and aerodynamic coefficients of the orbiter computed with the three different time steps during separation in the case with $l_{CoG}/l_o = 0.71$. All curves of these time steps display approximately the same variation tendency. Moreover, the values computed from the $dt \cdot U_\infty / l_b = 0.128\,2$ and $0.051\,28$ are closer to the feature points. Figure 5 shows the flowfield when the orbiter moves one of the approximately same positions during separation between different time step computations. The major flow structure is captured well and in the same between these flowfields, and the flowfields computed from $dt \cdot U_\infty / l_b = 0.128\,2$ and $0.051\,28$ are closer. Therefore, considering the computational cost and efficiency, the non-dimensional time step of $dt \cdot U_\infty / l_b = 0.1282$ is selected for numerical simulations.

D. Validations

1. Shock wave and laminar boundary layer interaction

SBLI is a typical and important phenomenon in two-body configurations at high speeds, so it is taken as an example. In this study, the numerical simulation results obtained with the same computational model and methods are compared with the measurement data obtained from an experiment in the LENS XX hypersonic wind tunnel
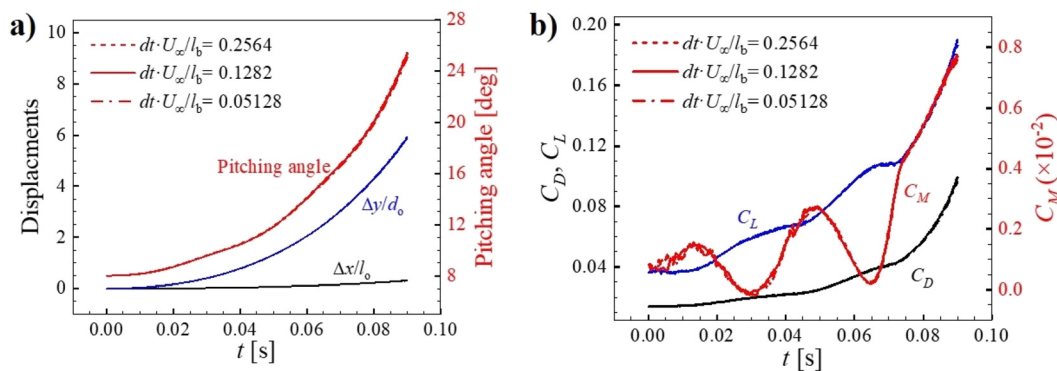

FIG. 4. Separation motion of the orbiter (a) and aerodynamic coefficients of the orbiter (b) in the $l_{CoG}/l_o = 0.71$ case in terms of different computational time steps.

a) $dt \cdot U_\infty / l_b = 0.2564$ **b)** $dt \cdot U_\infty / l_b = 0.1282$ **c)** $dt \cdot U_\infty / l_b = 0.05128$
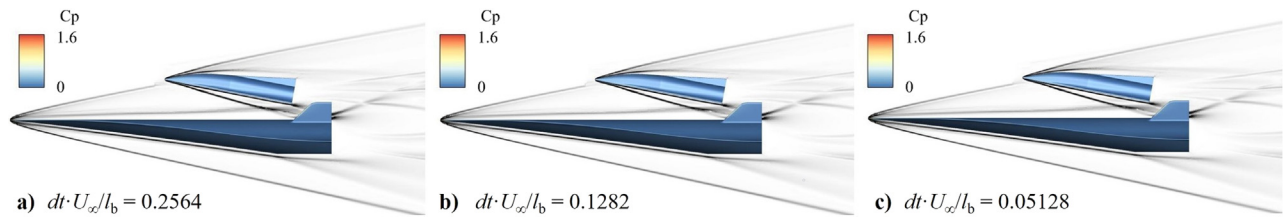
FIG. 5. Flowfields of the $t = 0.04$ s during separation in the $l_{CoG}/l_o = 0.71$ case in terms of different computational time steps.

at the Calspan University of Buffalo Research Center (CUBRC). Figure 6(a) shows the double-cone test model. The freestream conditions are $Ma = 12.2$, $Re = 1.4 \times 10^5$ m^{-1}, and $H_0 = 5.44$ MJ·kg^{-1}, which indicate a laminar flow pattern, and the uncertainty in the experimental measurements is $\pm 10\%$. More experimental details are depicted in Refs. 44 and 45. Figure 6(b) displays the computational flowfield around the double-cone, and Fig. 6(c) presents the comparison of the calculated surface pressure along the double-cone and measurement results. As shown in Fig. 6(c), a peak pressure discrepancy between CFD and measured data exists due to a transitional separated/reattached flow region, but the variation tendency of the pressure distributions between CFD and experiment is consistent. Moreover, the computationally separated flow region and location of the peak surface pressure are in good agreement with the measurement results. As a whole, the numerical method in the current study is acceptable.

2. Wing-pylon-store separation

The wing-pylon-store separation is one of the typical and standard experiment cases to validate the numerical simulation of multi-body separation with the dynamic mesh method.[46,47] The wing-pylon-store configuration is composed of a delta wing and a store, as shown in Fig. 7(a). The mass of the store is 907.8 kg, and the moments of inertia are $I_{xx} = 27.12$ kg·m^2, $I_{yy} = I_{zz} = 100$ kg·m^2. More details of the geometry and experiment are depicted in Ref. 46. The computational overset grid has 8.5 million grid cells and is shown in Fig. 7(b). The separation results are obtained with the overset grid method by computing the inviscid unsteady supersonic flow around the wing-pylon-store and numerically integrating 6-DOF motion equations. The

freestream conditions are $Ma = 1.2$, $Re = 7.87 \times 10^6$ m^{-1}, AoA $= 0$. Figures 7(c) and 7(d) show computational and experimental results of the displacements and Euler angles of the store during the separation. The computational displacements, pitching angle, and yaw angle are in good agreement with the experimental results, but a discrepancy is observed when $t > 0.4$ s for the roll angle. The reason for the discrepancy may be that the moment of inertia (I_{xx}) of the store in the rolling direction is smaller compared to the other moments of inertia (I_{yy} and I_{zz}), and the computational error may be amplified gradually. In general, the numerical method can accurately simulate the dynamic separation of the store. Moreover, the above two validation cases prove that the simulation methods in the current study can accurately simulate the complex aerodynamic interference and multi-body separation and, therefore, can be applied to the numerical study of the stage separation of TSTO at high speeds.

IV. RESULTS AND DISCUSSIONS
A. Interference mechanism and aerodynamics before separation

The initial stage separation condition describes the mutual interference and aerodynamics of the stages that will determine the subsequent separation behavior and flow patterns before orbiter release. As shown in Fig. 8, the flow structures are characterized by the type VI SSI of the booster leading edge shock S1 and orbiter shock S2, the S2-induced boundary layer separation, large-scale horseshoe vortex structure between the stages, and a downstream wake vortex system associated with compression shock waves. The vortex isosurface shown in the results is described by the LiutexUTA method, which is implemented by the LiutexUTA code published by Liu at the University of Texas at Arlington.[48,49] In addition, S2 interacts with the
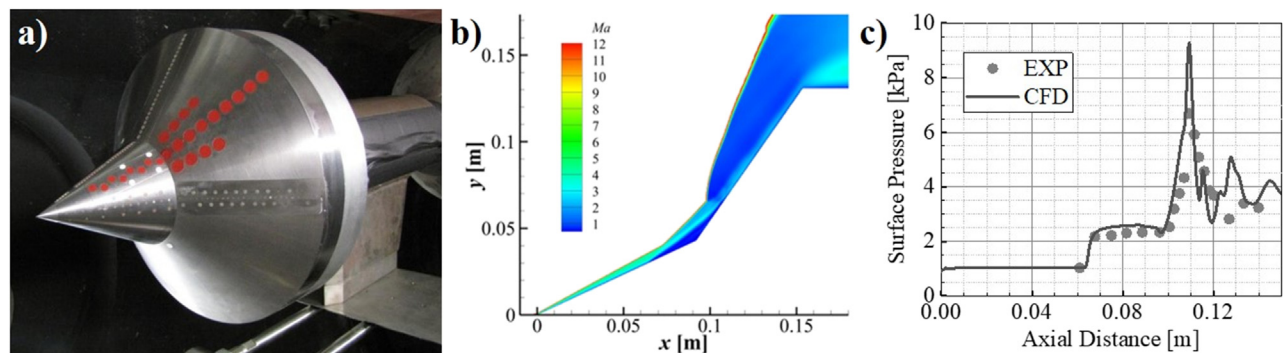

FIG. 6. Shock wave and laminar boundary layer interaction: (a) double-cone test model, (b) computational flowfield (Mach number contour), and (c) surface pressure distribution on the double-cone: experimental and CFD results.
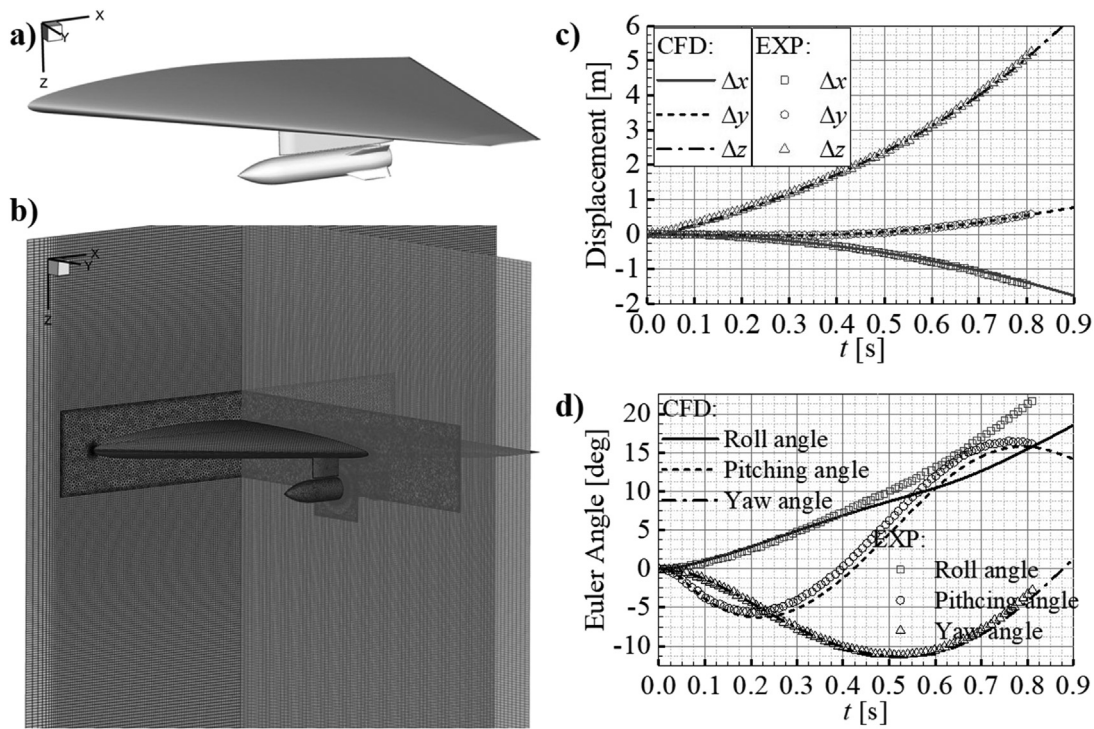
FIG. 7. Wing-pylon-store separation: (a) geometry, (b) computational overset grid, (c) and (d) computational and experimental displacements and Euler angles of the store during the separation.
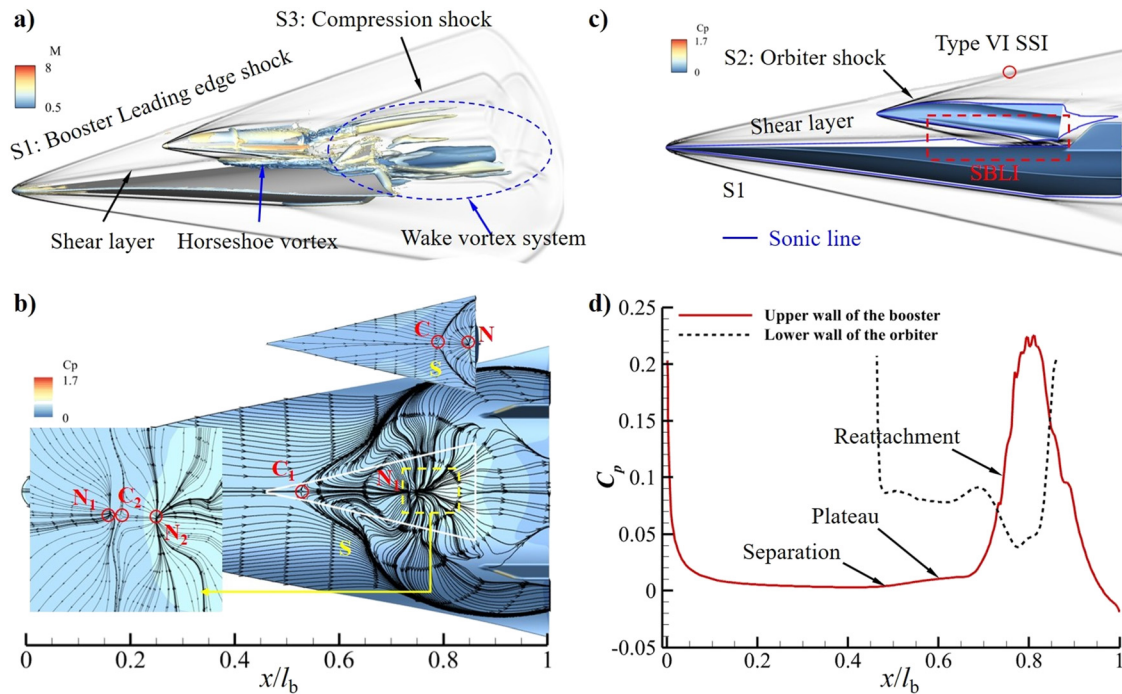

FIG. 8. Flowfield of TSTO before separation: (a) symmetry numerical schlieren and vortex structure illustrated by Liutex magnitude of 8000 and colored by Mach number contour; (b) skin-friction lines and pressure coefficient contours on the stage walls; (c) sketch of aerodynamic interference between stages; and (d) sketch and illustration of the pressure coefficients along the stage walls in the symmetry plane.

boundary layer on the booster, and the resulting adverse pressure gradient propagates upstream in the subsonic layer, causing the boundary layer to separate and become a shear layer interacting with S2. Due to the weakness of the incident shock S2, the separation point shifts upstream and is located at $x/l_b = 0.5$, and the plateau pressure increases slightly, as shown in Figs. 8(c) and 8(d). However, the reattachment of the boundary layer causes a rapid pressure increase and induces a reattachment shock. This reattachment shock impinges on the lower wall of the orbiter, and therefore, the peak pressure is located on the aft body of the orbiter, as shown in Fig. 8(d). Furthermore, the adverse pressure gradient originating from the lower wall of the orbiter induces the boundary layer to separate into a shear layer, which impinges on the upper wall of the booster, resulting in the peak pressure and secondary flow separation, as shown in Figs. 8(d) and 8(b), respectively. In addition, the separation topology shown in Fig. 8(b) presents two recirculation regions on the upper wall of the booster and one recirculation region on the lower wall of the orbiter. The primary recirculation region is formed by the incident shock S2-induced boundary layer separation and stretches from the saddle point C_1 to the attachment node N_1. The secondary recirculation region is the area from the saddle point C_2 to the attachment node N_2. Due to the weaker interaction between the separated shear layer on the lower wall of the orbiter and the reattachment boundary layer on the booster, the secondary recirculation zone is smaller than the primary one. Additionally, the interaction of the reattachment shock wave and the orbiter boundary layer results in the flow separation on the lower wall of the orbiter from saddle point C to the attachment node N. As shown in Fig. 8(d), the valley pressure on the lower wall of the orbiter is due to the effect of the expansion waves formed during the reattachment of the boundary layer in the S2-induced SBLI. As the supersonic flow passed through the small area enveloped by the separated boundary layer of the orbiter and into the expansion channel, as shown in Fig. 8(c), the flow accelerates, and the pressure decreases along the booster aft body, as shown in Fig. 8(d). The flow structure and the separation topology, i.e., the skin-friction lines on the booster, are similar to those in the previous study[17] and the study on the SANGER configuration.[50]

Figure 9 shows the relationship between the orbiter's pitching moment coefficients and its CoG positions. The pitching moment coefficient presents a linear variation with the l_{CoG}/l_o and satisfies the equation $C_M = al_{CoG}/l_o + b$. This relationship is related to the simplified function $M_z = L(l_{CoG} - l_{CoP})$, where M_z is the pitching moment,
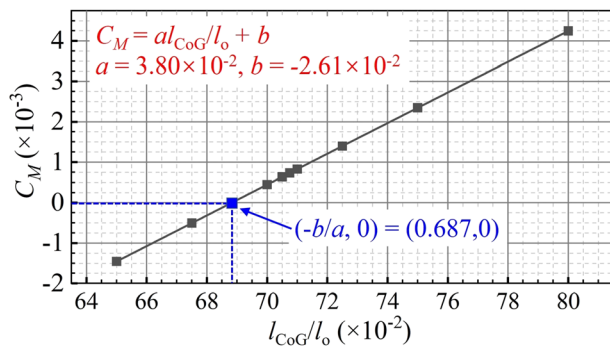

FIG. 9. Variation of pitching moment coefficient of the orbiter with the CoG.

L is the lift force, and l_{CoP} is the longitudinal position of the center of pressure (CoP) on the orbiter. The pitching moment increases with the rearward shift of the CoG. A positive value of the moment indicates a nose-up moment, while a negative value indicates a nose-down moment. As shown in Fig. 9, the pitching moment equals zero when $l_{CoG}/l_o = 0.687$, suggesting that the CoP is located at $l_{CoP}/l_o = 0.687$ before separation. Moreover, if the CoP is in front of the CoG, a nose-up moment is exerted on the orbiter; otherwise, a nose-down moment is exerted. Therefore, if $l_{CoG}/l_o < 0.687$, a nose-down moment is exerted on the orbiter before separation, and therefore, the orbiter will fly nose-down and collide with the booster, leading to separation failure; in contrast, if $l_{CoG}/l_o > 0.687$, a nose-up moment is exerted on the orbiter, and therefore, the obiter will fly nose-up and safely separate from the booster. However, due to the complex aerodynamic interference and coupling of the flow and body during stage separation, it would not be easy to claim the appropriate CoG condition for safe separation based on the initial aerodynamics, as discussed in Secs. IV B and IV C.

B. Dynamic behavior and aerodynamics during separation

Figure 10 illustrates the separation trajectories and speeds of the orbiter during stage separation under different CoG conditions, respectively. Based on the variation trends of these curves, the separation behaviors varying with the CoG are divided into three scenarios. In the cases of $l_{CoG}/l_o \leq 0.70$, the displacements and the velocities have the same variation tendency. Specifically, the longitudinal displacements and velocities increase monotonically and steadily; the pitching angle and angular velocity decrease monotonically and steadily; the transverse displacement and velocity first increase and then decrease. In particular, the longitudinal motions in the cases of $l_{CoG}/l_o < 0.70$ vary asymptotically to the longitudinal displacement in the case of $l_{CoG}/l_o = 0.70$. Furthermore, as the separation progresses, the orbiter will fall toward the booster after reaching the highest position relative to the booster with a decreasing pitching angle, i.e., the orbiter will fly nose-down to the booster, resulting in collision and separation failure. In the case of $l_{CoG}/l_o > 0.70$, the velocities increase faster and faster as the separation progresses, and therefore, the displacement also increases at an accelerating rate. The pitching motion of the orbiter varies continuously with the increase. As such, the orbiter successfully separates from the booster with its nose pointing upward. It can be concluded that $l_{CoG}/l_o = 0.70$ divides the separation behaviors in the investigated cases of $0.65 \leq l_{CoG}/l_o \leq 0.80$ into two scenarios. With the backward shift of the CoG, the motion variables shown in Fig. 10 tend to increase gradually at the same separating instants, especially in the cases of $0.75 < l_{CoG}/l_o \leq 0.80$. As can also be seen from Fig. 10, the orbiter's displacements and velocities vary dramatically in the case of $l_{CoG}/l_o = 0.80$, while $t > 0.04$ s. The pitching angular speed increases at an accelerating rate during the separation, and therefore, the pitching angle increases rapidly, leading to the stalling and somersault of the orbiter, which signify the stage separation failure, as shown by the "reverse" of the pitching angle from 180° to −180° in Fig. 10(c). The third scenario of the stage separation behavior is represented by the case of $l_{CoG}/l_o = 0.80$; i.e., the orbiter separates from the booster but with stalling and pitching somersault, which is another type of separation failure. Figure 11 presents the snapshots at some instants in several typical stage separation cases
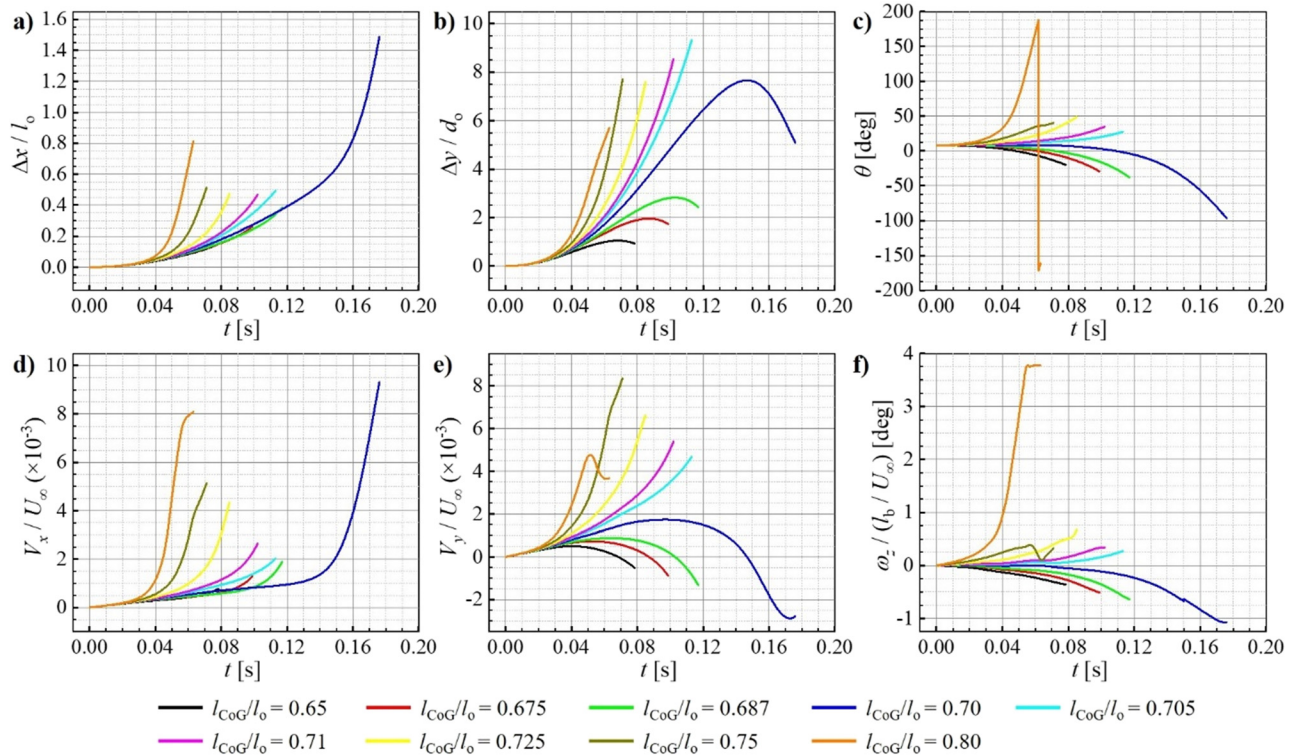
FIG. 10. Time history of the displacements and speeds of the orbiter in the simulations of stage separation at different CoG conditions: (a) longitudinal displacement, (b) transverse displacement, (c) pitching angle, (d) longitudinal speed, (e) transverse displacement, and (f) pitching angular speed.

to show three scenarios of the separation behavior mentioned above. Figures 11(a)–11(c) represent the first scenario, i.e., $0.65 \leq l_{CoG}/l_o \leq 0.70$, in which the orbiter was first lifted up but with a decreasing pitching angle and then flew nose-down, resulting in the collision of two stages. Figures 11(d)–11(f) represent the second scenario, i.e., $0.705 \leq l_{CoG}/l_o \leq 0.75$, in which the orbiter successfully separates from

the booster. Figure 11(g) represents the third scenario, i.e., $l_{CoG}/l_o = 0.80$, in which the orbiter performs a pitching somersault. It is found that the second scenario of stage separation may be favorable for the successful stage separation of the TSTO vehicle, while the others should be avoided. However, more detailed flow physics and associated aerodynamic effects on the stage separation should be further
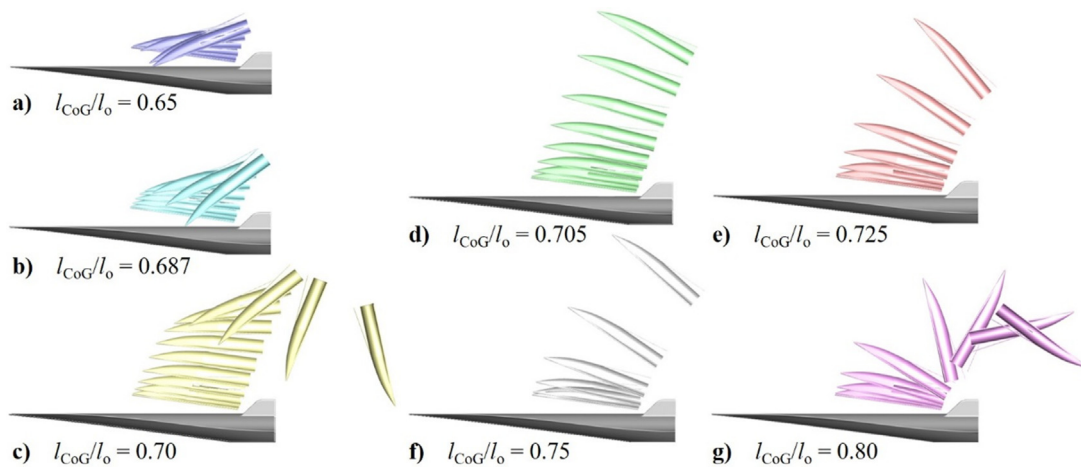

FIG. 11. Sequences of the relative positions between stages during stage separation in different CoG cases.

analyzed to determine the specific condition of CoG for absolutely safe TSTO vehicle separation.

Figure 12 illustrates the longitudinal aerodynamic coefficients, including C_D, C_L, and C_M, of two stages during the separation. These aerodynamic coefficients are calculated by Eqs. (19)–(21), where "$*$" is replaced by "o" and "b" for the orbiter and the booster, respectively. Here, D is the drag, and M_z is the pitching moment, indicating the nose-up moment when $M_z > 0$ and the nose-down moment when $M_z < 0$. In general, in the stage separation, the non-dimensional aerodynamics of the orbiter are larger than those of the booster, which indicates the orbiter would be more markedly affected by the aerodynamic interaction in the stage separation of the TSTO in the current research. This is in agreement with the result of the study of Wang et al., who numerically investigated the aerodynamic interference between the TSTO-like two-body configuration.[17] Additionally, the range and the variation of the aerodynamics of the two stages tend to be larger and show more significant fluctuation with the backward shift of the CoG. Moreover, the aerodynamics of the two stages in the cases of $l_{CoG}/l_o = 0.75$ and 0.80 show variation tendencies different from those in the other cases.

As for the orbiter, the drag steadily increases when $l_{CoG}/l_o < 0.75$ while first increasing steeply and then decreasing rapidly with $l_{CoG}/l_o = 0.75$ and 0.80. The lift decreases to negative values, eventually causing the orbiter downward to the booster when $0.65 \leq l_{CoG}/l_o \leq 0.70$ while increasing monotonically when $0.70 < l_{CoG}/l_o < 0.725$. When $0.725 \leq l_{CoG}/l_o \leq 0.80$, the lift first increases and then decreases

rapidly even to negative values with $l_{CoG}/l_o = 0.80$. Moreover, the pitching moment varies steadily if $l_{CoG}/l_o < 0.725$ in contrast to the large amplitude and fluctuation when $l_{CoG}/l_o \geq 0.725$. Particularly, the pitching moment decreases to the nose-down moment when $0.65 \leq l_{CoG}/l_o \leq 0.70$, while a small nose-up moment is maintained in the stage separation when $0.705 \leq l_{CoG}/l_o < 0.725$. Thus, the orbiter separates from the booster smoothly without a great altitude change under the positive lift and proper nose-up moment with $0.705 \leq l_{CoG}/l_o < 0.725$, as shown in Figs. 11(d) and 11(e). However, the orbiter downwards and nose-downs to the booster under the negative lift and nose-down moment when $0.65 \leq l_{CoG}/l_o \leq 0.70$, as shown in Figs. 11(a)–11(c). In the meantime, since the orbiter is subjected to greater forces and pitching moment during stage separation with larger l_{CoG}/l_o, the velocity is higher, and the linear and angular displacements are larger, as shown in Fig. 10. Consequently, the orbiter would separate from the booster with a large pitching angular speed and angle in the cases of the $0.725 \leq l_{CoG}/l_o \leq 0.80$. The orbiter separates from the booster when $0.75 \leq l_{CoG}/l_o \leq 0.80$, though turning a somersault eventually and separating unsuccessfully due to the much higher pitching moment, as shown in Fig. 12(c). Additionally, the orbiter's aerodynamics and stage separation behavior prove that the critical point of the CoG for the successful stage separation is located at $l_{CoG}/l_o = 0.70$ instead of the initial CoP location of $l_{CoG}/l_o = 0.687$. The orbiter would be nose-down and collide with the booster if $l_{CoG}/l_o \leq 0.687$ because the initial CoP is behind the CoG. However, the orbiter could also be nose-down to the booster if $l_{CoG}/l_o \geq 0.687$, where the initial CoP is
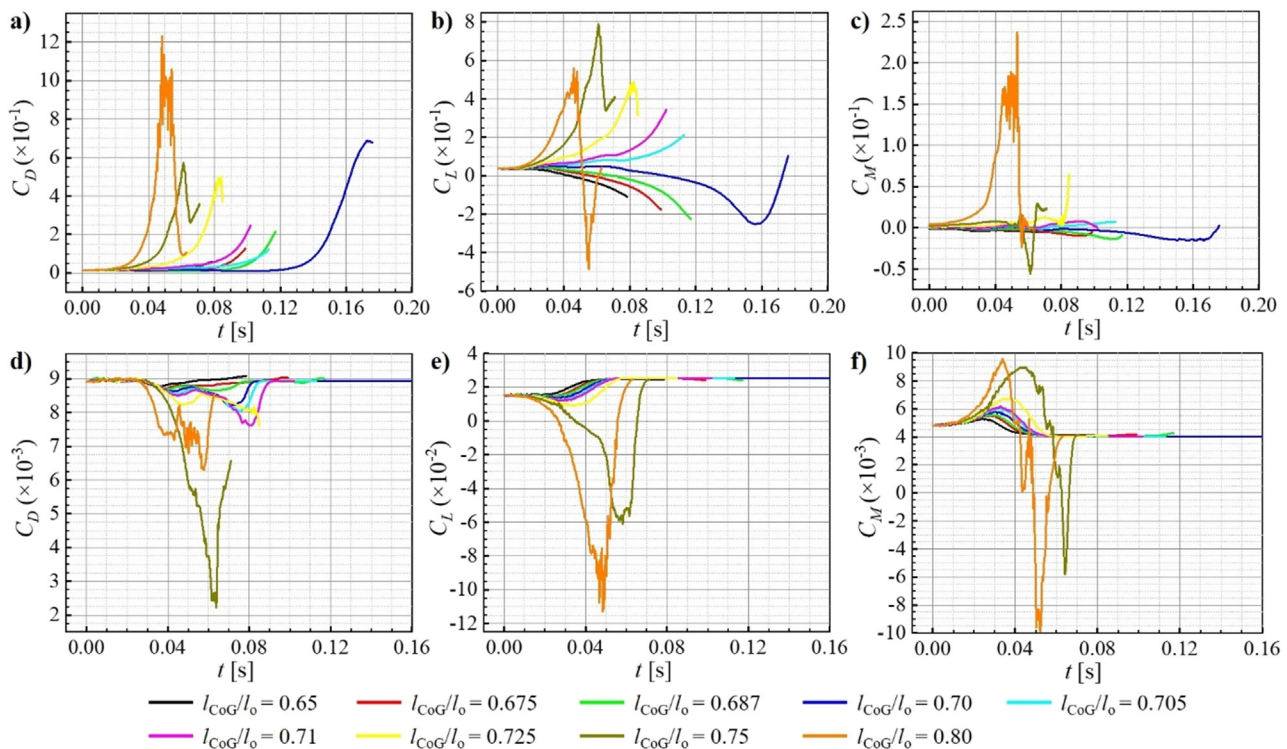

FIG. 12. Time history of the aerodynamic coefficients of the stages during stage separation with different CoG cases: subfigures (a)–(c), the orbiter; subfigures (d)–(f), the booster.

ahead of the CoG, e.g., $0.687 \leq l_{CoG}/l_o \leq 0.70$ that is caused by the subsequent complex aerodynamic interaction between the stages. Therefore, the mutual interaction effect between the orbiter's movement and the aerodynamics in the stage separation is significant and will be discussed further

$$C_D = \frac{D}{\frac{1}{2}\rho_\infty U_\infty^2 l_* w_*}, \quad (19)$$

$$C_L = \frac{L}{\frac{1}{2}\rho_\infty U_\infty^2 l_* w_*}, \quad (20)$$

$$C_M = \frac{M_z}{\frac{1}{2}\rho_\infty U_\infty^2 l_*^2 w_*}. \quad (21)$$

As for the booster, the aerodynamic variations during stage separation follow the same tendency, i.e., the drag and the lift first steadily decrease and then increase to the undisturbed values, while the pitching moment first decreases and then decreases to the undisturbed values. However, with $0.75 \leq l_{CoG}/l_o \leq 0.80$, the forces and the moments show large fluctuations, possibly leading to high risks, e.g., the lift drops sharply to negative values like the stalling of airplanes, and the pitching moment first shows a higher increase and then drops steeply to a nose-down moment and quickly recovers to the undisturbed value. These drastic changes in the aerodynamics of the booster pose a potential risk to flight stability during stage separation, even if the booster is fixed in the current simulation. The complex flow physics accounting for such unusual and anomalous aerodynamics of the two stages will be analyzed further later. Now, based on the analysis of the stage separation behavior and aerodynamics of both stages with different CoG cases, the second group of stage separation cases with $0.705 \leq l_{CoG}/l_o \leq 0.75$ would be the indulgent condition for the safe separation of the obiter if ignoring the booster's aerodynamic characteristics. However, taking the booster into account, the safe stage separation condition in terms of CoG for the TSTO vehicle is $0.705 \leq l_{CoG}/l_o < 0.75$.

C. Unsteady interference mechanisms governing the separation

1. Collision of the two stages ($0.65 \leq l_{CoG}/l_o \leq 0.70$)

Collision of the two stages is the most serious accident during TSTO stage separation, which affects the survival and reusability of both stages. Figures 11(a)–11(c) show three failures in the first group of the orbiter, which eventually moves toward the booster. The orbiter is nearly under the nose-down moment and decreases the pitching angle when $0.65 \leq l_{CoG}/l_o \leq 0.70$. Figure 13 shows the orbiter's pitching moment coefficients during stage separation with $0.65 \leq l_{CoG}/l_o \leq 0.70$, and two sequences of several feature points on the curves are marked to analyze the aerodynamic interaction during stage separation. These feature points are in the one-to-one correspondence instants discussed in the following subgraph of Figs. 14–18. Due to the similar variation trends of the pitching moment when $0.65 \leq l_{CoG}/l_o \leq 0.687$ and distinct variation of that when $l_{CoG}/l_o = 0.70$, the pitching moment and the associated aerodynamic interaction when $l_{CoG}/l_o = 0.687$ and 0.70 will be discussed as representative cases.
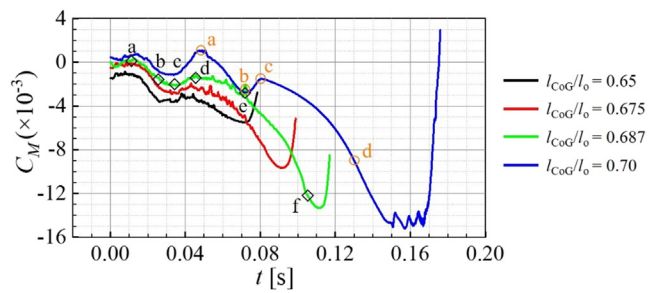

FIG. 13. Time history of the orbiter's pitching moment coefficients during stage separation with $0.65 \leq l_{CoG}/l_o \leq 0.70$: the diamonds represent the feature points analyzed with $l_{CoG}/l_o = 0.687$, while the circles represent the feature points analyzed with $l_{CoG}/l_o = 0.70$.

Figures 14 and 15 present several typical instants of the flowfield of TSTO with $l_{CoG}/l_o = 0.687$ to analyze the mechanism between the aerodynamic interaction and the collision. Figure 16 illustrates the variation of wall pressure coefficient distribution along the stages between these instants during stage separation. The main flow structure between the two stages at $t = 0.012$ s in Figs. 14(a) and 15(a) is the same as that at $t = 0$ s, with type VI SSI. The incident orbiter shock S2 induced the booster boundary layer separation and a horseshoe vortex, and the reattachment shock S4 impinged on the orbiter rearward and induced flow separation from the rearward. Therefore, the wall pressure distribution responses are similar. The takeoff position of the pressure on the booster due to boundary layer reattachment shifts downstream as the orbiter separates, as shown in Fig. 16(a), and the pressure rises on the orbiter rearward are smaller than that at $t = 0$ s, as shown in Fig. 16(b), as reattachment shock S4 impinges on its aft. Due to the smaller pressure distribution on the rearward lower wall of the orbiter, the nose-down moment minimizes, i.e., point "a" on the green curve in Fig. 13. As the orbiter separates, reattachment shock S4 no longer impinges on the orbiter and interacts with the compression shock of type I SSI in the wake, as shown in Figs. 14(b)–14(d). As a result, the high pressure on its afterbody disappears, but the peak pressure value exits on the lower wall of the orbiter when $t \leq 0.034$ s, as shown in Fig. 16(b). The supersonic airflow under the orbiter nose flows over orbiter shock S2 with the reduction of the flow channel area due to the incidence of the orbiter and the bulging of the booster boundary layer due to SBLI. As a result, the supersonic flow pressure increases as the flow speed decreases. The convergence of the flow channel does not change apparently as the orbiter moves when $t \leq 0.034$ s, so the peak value at the lower wall of the orbiter is almost the same, as shown in Fig. 16(b). Moreover, the decelerated airflow passes through the expansion waves appearing where the boundary layer reattaches, so that the airflow accelerates and the flow pressure decreases downstream, as shown by the "valley" in Fig. 16(b). Furthermore, the nose-down moment of the orbiter increases as the high-pressure zone shifts downstream cross the CoG, maximizing at $t = 0.034$ s, i.e., point "c" on the green curve in Fig. 13. As the orbiter separates away further, as shown in Fig. 14(d), the interstage gap increases enough, so the lower wall of the orbiter does not suffer from the interaction caused by SBLI on the booster. The high pressure on the lower wall of the orbiter vanishes, resulting in the nose-down moment of the orbiter minimizing, as shown by point "d" on the green
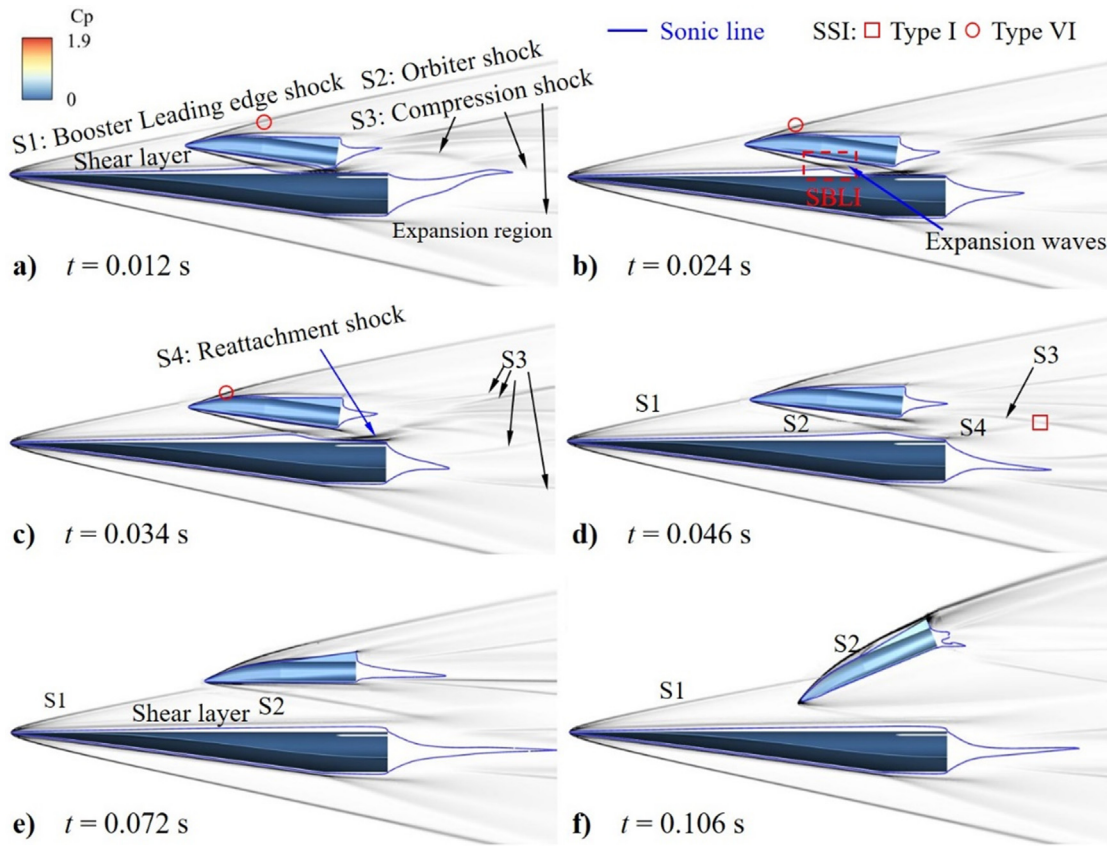
FIG. 14. Numerical schlieren and sonic line on the symmetry plane and wall pressure contour of several feature instantaneous flowfields during stage separation in the representative condition with $l_{CoG}/l_o = 0.687$.

curve in Fig. 13. The orbiter is under the action of the nose-down moment, whose pitching angle is decreasing during stage separation, and the pressure on the lower wall of the orbiter is decreasing while that on the upper wall around the nose is increasing, as shown in Figs. 16(b) and 16(c). Consequently, its lift force and pitching moment decrease after $t = 0.034$ s. Moreover, the orbiter cannot pass through the cover of the booster leading edge shock S1, as shown in Figs. 14(e) and 14(f), and the impinging of S1 on the orbiter nose induces the high rise of the pressure and then causes the orbiter to nose-down

toward the booster. Finally, the collision occurs. Additionally, the flow along the lower wall of the orbiter separates and induces the streamwise vortex, as shown in Fig. 15(c), resulting in the lower pressure distribution, as shown in Fig. 16(b).

As for the booster, on the other hand, the horseshoe vortex on the booster shifts downstream and diminishes when $t \leq 0.034$ s, as shown in Fig. 15(b), until vanishing with the disappearance of SBLI, and the pressure variation behavior on the upper wall of the booster in Fig. 16(a) is thoroughly analyzed as follows. At first, a length L_s typical
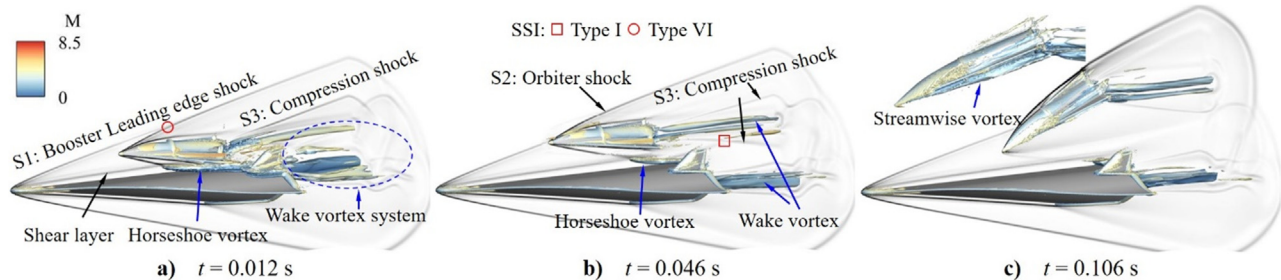

FIG. 15. Numerical schlieren on the symmetry plane and vortex structure illustrated by isosurface of Liutex magnitude of 8000 and colored by Mach number of three representative flowfields during stage separation with $l_{CoG}/l_o = 0.687$.
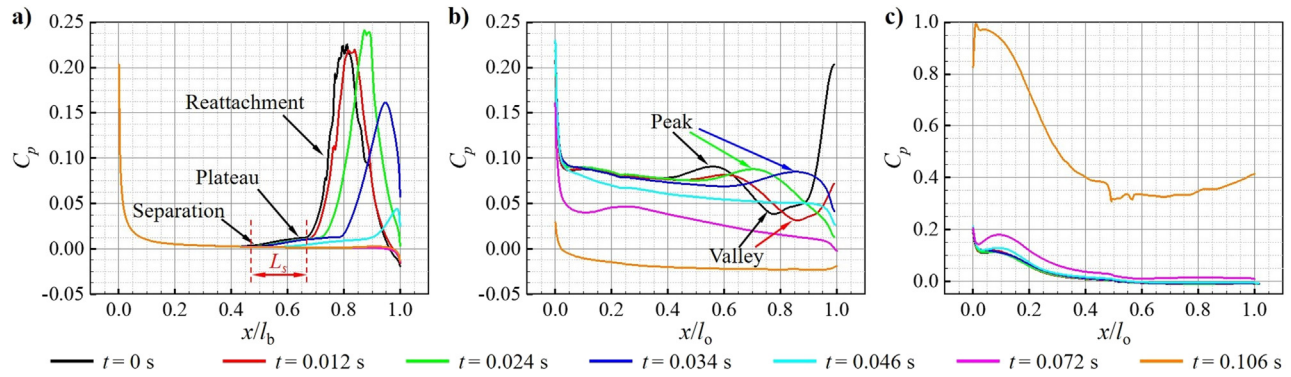
FIG. 16. Pressure coefficient distributions along the stage walls at several instants during stage separation with $l_{CoG}/l_o = 0.687$: (a) upper symmetry line on the booster, (b) lower symmetry line on the orbiter, and c) upper symmetry line on the orbiter.

of interaction streamwise for convenience discussion is defined as the distance between the separation point and the end of the pressure plateau, as shown in Fig. 16(a). As the orbiter moves, the inviscid incidence position and the strength of the orbiter shock S2 shift downstream and decrease slightly, and L_s steadily increases when $t \leq 0.034$ s. During this process, the incidence shock gradually weakens, but the local Reynolds number Re_δ of the incidence position increases with the boundary layer development along the wall, where δ is the displacement thickness of the boundary layer. When Re_δ < 10^5, since the relative importance of the viscous forces decreases with increasing Re_δ, the free-interaction theory predicts an increase in the interaction extent and a decrease in the overall pressure rise with

increasing Reynolds number. One consequence of such a laminar regime is that the larger value L_s can be achieved at a larger Reynolds number with the same strength of incident shock in the shock-induced separation, even if the strength of the orbiter shock S2 decreases slightly. The results shown in Fig. 14(a) when $t \leq 0.034$ s agree well with the free-interaction theory as long as $Re_\delta < 10^5$, where the predominance of viscosity is apparent to resist the separation induced by the adverse pressure gradient in laminar flows.[51] Moreover, a greater decrease in the reattachment pressure rise at $t = 0.046$ s is observed due to the weakness of the incidence shock S2 compared to that when $t \leq 0.034$ s due to the decreasing pitching angle of the orbiter. As the high-pressure zone induced by SBLI on the
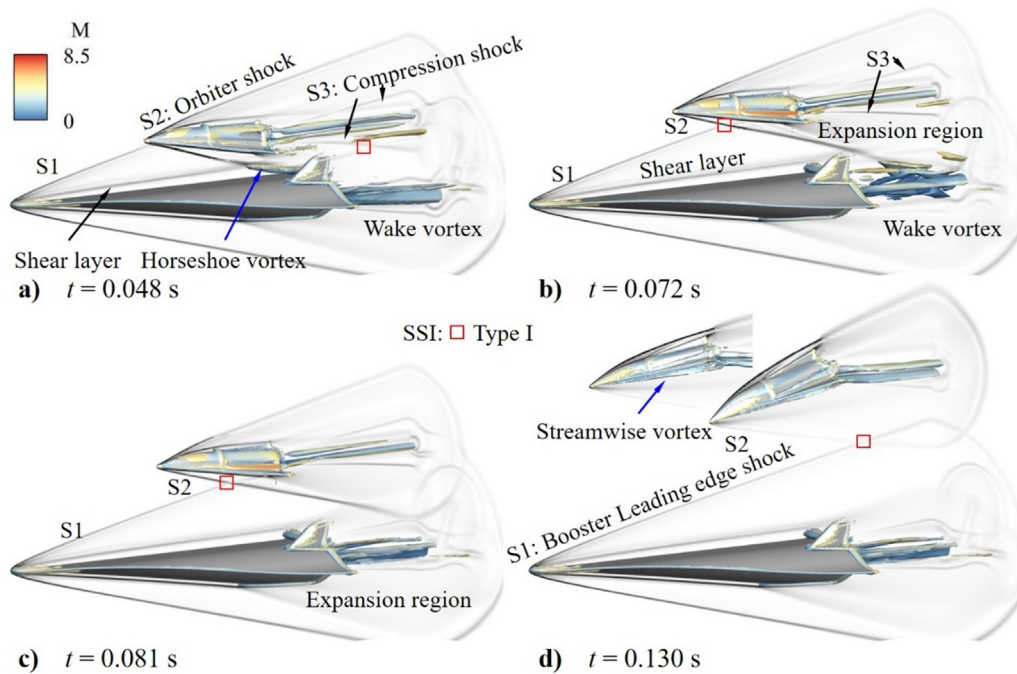

FIG. 17. Numerical schleiren on the symmetry plane and vortex structure illustrated by isosurface of Liutex magnitude of 8000 and colored by Mach number of several feature instantaneous flowfields during stage separation with $l_{CoG}/l_o = 0.70$.
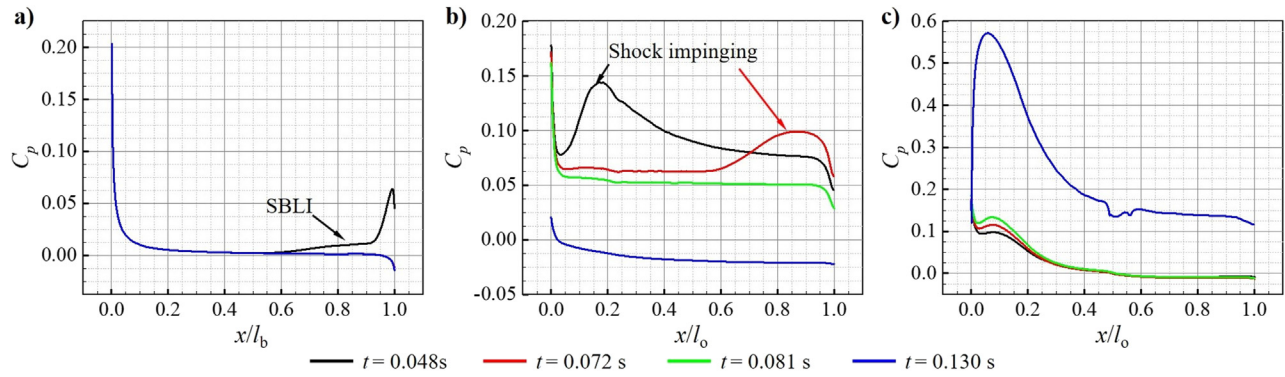
FIG. 18. Pressure coefficient distributions along the stage walls at several instants during stage separation with $l_{CoG}/l_o = 0.70$: (a) upper symmetry line on the booster, (b) lower symmetry line on the orbiter, and (c) upper symmetry line on the orbiter.

booster moves downstream over the CoG and with decreasing magnitude, the lift force increases to the undisturbed status when SBLI disappears, and the nose-up moment increases first and then decreases to the undisturbed status, as shown in Figs. 12(e) and 12(f).

Figures 17 and 18 show several typical instants of the flowfields and the pressure coefficient along the stage walls during stage separation with $l_{CoG}/l_o = 0.70$. The flowfield and aerodynamics before instant a, i.e., $t < 0.048$ s when the orbiter has not passed across the booster leading edge shock S1, are similar to those with $l_{CoG}/l_o = 0.687$ when $t \leq 0.046$ s, as shown in Figs. 14 and 15. As shown in Fig. 17(a), the booster leading-edge shock impinges on the underneath nose of the orbiter, resulting in the high-pressure rise, as shown in Fig. 18(b). Thus, the orbiter nose-up moment maximizes, as shown by point "a" on the blue line in Fig. 13. In addition, orbiter shock S2 induces the flow separation, e.g., the horseshoe vortex appears on the rearward of the booster, and the pressure rise is shown in Fig. 18(a). As the orbiter separates, S1 intersects with S2 in type I SSI, and the location of the transmitted shock impinging on the lower wall of the orbiter shifts from forward to rearward, as does the high-pressure rise, causing the pitching moment to gradually switch from the nose-up moment to nose-down moment. Finally, the nose-down moment maximizes, as shown by point "b" in Fig. 13, when the transmitted shock impinges on the rearward of the orbiter, as shown in Fig. 17(b). Moreover, the transmitted shock of S2 no longer incidents to the booster but the wake behind the booster, resulting in stretching and deformation of the wake vortex. Figure 17(c) shows that the transmitted shock of S1 impinges on the trailing edge of the orbiter, and the pressure along the lower wall of the orbiter does not show any pressure rise, as shown in Fig. 18. Thus, the nose-down moment minimizes, as shown by point "c" on the blue line in Fig. 13. The orbiter manifests nose-down separating behavior shown in Fig. 17(d), and the pressure along the upper wall of the orbiter increases while that along the lower wall decreases due to the flow separation, e.g., the streamwise vortex shown in Fig. 18(c). The nose-down moment continues to increase further, as shown in Fig. 13. Finally, the orbiter falls into the wake of the booster, indicating the failure of TSTO stage separation.

In general, the failure of TSTO stage separation with the orbiter nose-down to the booster when $l_{CoG}/l_o \leq 0.687$ and $l_{CoG}/l_o = 0.70$ is due to the different aerodynamic interaction mechanisms. The former is due to the nose-down moment contributed by SBLI occurring in the

clearance near the rearward orbiter, but the latter is due to the pitching moment switching from nose-up to nose-down moment as the impingement point of the booster leading-edge shock on the orbiter shifts downstream along the lower wall of the orbiter. The orbiter cannot balance or compensate for such a nose-down moment because of the relatively forward CoG.

2. Successful stage separation of the two stages ($0.705 \leq l_{CoG}/l_o \leq 0.725$)

Figure 19 illustrates the time history of the orbiter's pitching moment coefficient during stage separation with $0.70 \leq l_{CoG}/l_o \leq 0.725$ and several feature points to be discussed. The pitching moment coefficients before instant "c" vary at the same trend between these conditions, possibly indicating that the aerodynamic interactions dominated by SSI and SBLI around the two stages are the same. At an instant, C_M maximizes at point "a," where the booster leading-edge shock S1 impinges on the lower wall of the orbiter nose, as shown in Fig. 17(a). Thus, the nose-up moment increases. Then, C_M minimizes at point "b," where the transmitted shock of S1 impinges on the afterbody of the orbiter, as shown in Fig. 17(b). Thus, the nose-down moment increases. Next, C_M reaches inflection point "c," where S1 no longer interacts with the orbiter, as shown in Fig. 17(c). Figure 20 shows the flowfields of several feature instants in Fig. 19 to demonstrate the similarity and difference of these instantaneous flowfields
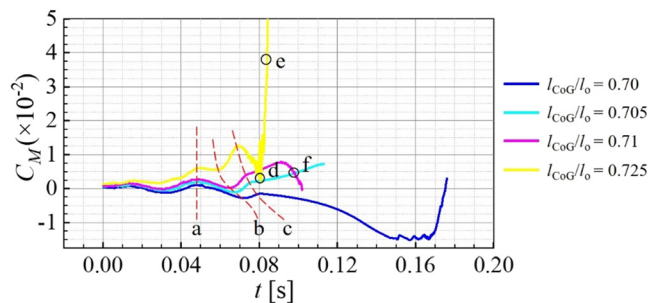

FIG. 19. Time history of the pitching moment coefficient of the orbiter during stage separation with $0.70 \leq l_{CoG}/l_o \leq 0.725$ and several marked feature points.
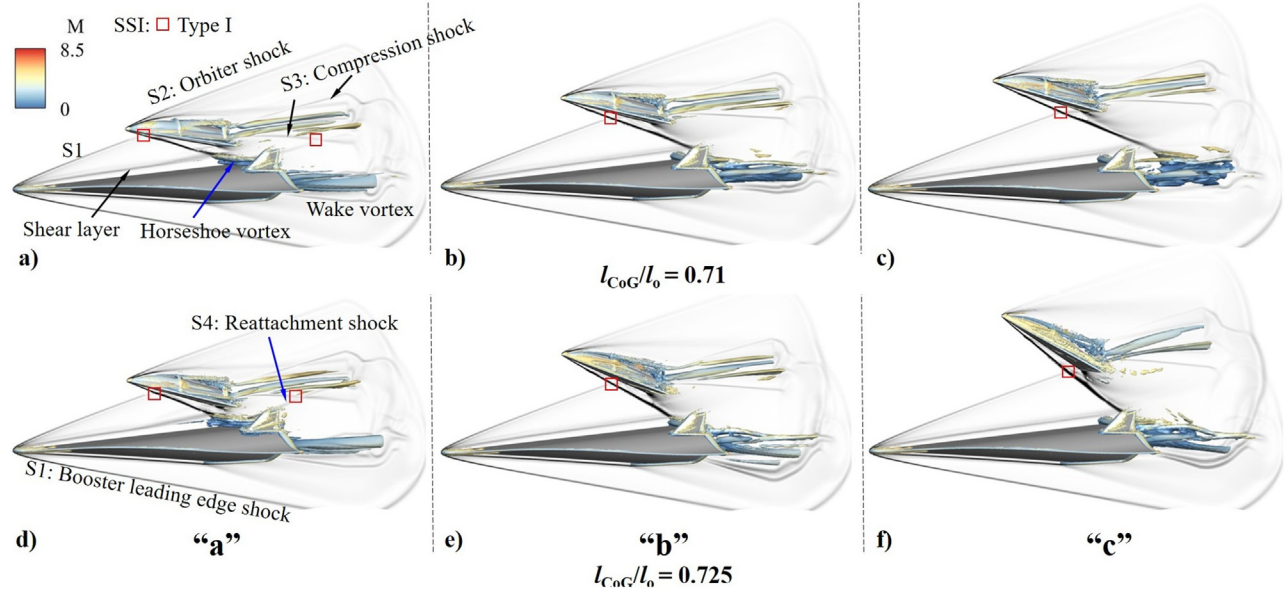
FIG. 20. Numerical schlieren on the symmetry plane and vortex structure illustrated by isosurface of Liutex magnitude of 8000 and colored by Mach number of feature instantaneous flowfields of "a," "b," and "c" during stage separation with $l_{CoG}/l_o = 0.71$ and 0.725.

before instant "c" between the condition with $0.70 \leq l_{CoG}/l_o \leq 0.725$. The shock structures between these flowfields are the same as those in the previous description. In addition, the orbiter presents a greater pitching angle under conditions with larger l_{CoG}/l_o hence the stronger orbiter shock S2. Consequently, the pressure rise and separation area on the booster due to the interaction of S2 and boundary layer are larger, and the pressure along the orbiter's windward wall increases, whereas the pressure along the orbiter's leeward wall decreases, as shown in Fig. 21. Furthermore, with greater pitching angles of the orbiter during stage separation, the consequent pressure difference between the lower and upper walls of the orbiter increases, which would further increase due to the S2 impinging on the orbiter, resulting in the larger pitching moment in conditions with larger l_{CoG}/l_o, as shown in Fig. 19. However, an anomalous phenomenon of the

pitching moment is observed with $l_{CoG}/l_o = 0.71$, where the nose-up moment decreases but increases with $l_{CoG}/l_o = 0.705$, as shown by point "f" in Fig. 19. Figures 22(a) and 22(b) show the two flowfields at instant "f" under the conditions that $l_{CoG}/l_o = 0.705$ and 0.71, where the flow patterns are the same, but the orbiter presents a greater pitching angle with $l_{CoG}/l_o = 0.71$. Thus, the expansion waves originate from the afterbody of the orbiter closer to the orbiter shock, indicating that the high pressure on the rearward of the orbiter's lower wall needs to expand and decreases sooner in the wake. Therefore, the nose-up moment of the orbiter under the condition that $l_{CoG}/l_o = 0.71$ decreases. The effect would be more complex under conditions with larger l_{CoG}/l_o. For example, the high pressure on the rearward of the lower wall of the orbiter induces the adverse pressure gradient and propagates upstream, resulting in the variation and movement of the
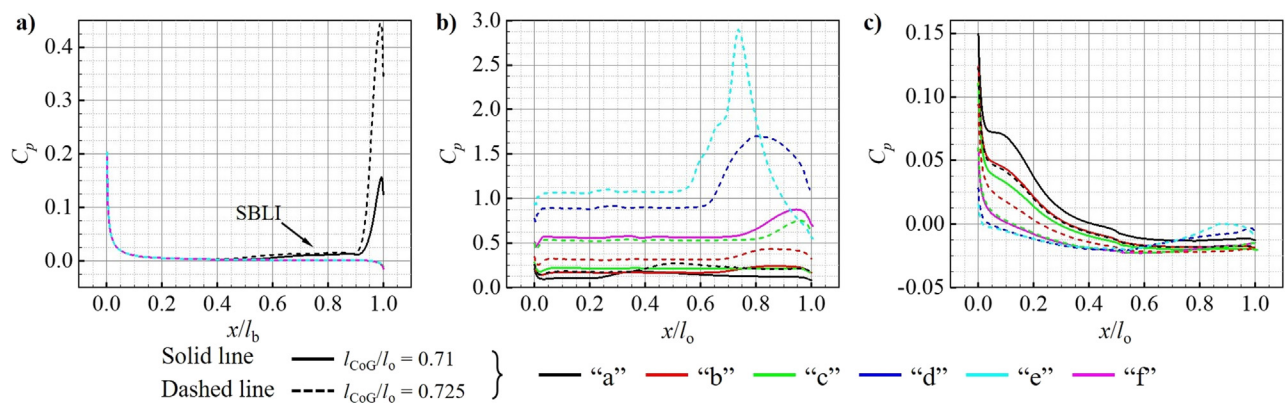

FIG. 21. Pressure coefficient distributions along the stage walls at several instants during stage separation with $l_{CoG}/l_o = 0.71$ and 0.725: (a) upper symmetry line on the booster, (b) lower symmetry line on the orbiter, and (c) upper symmetry line on the orbiter.
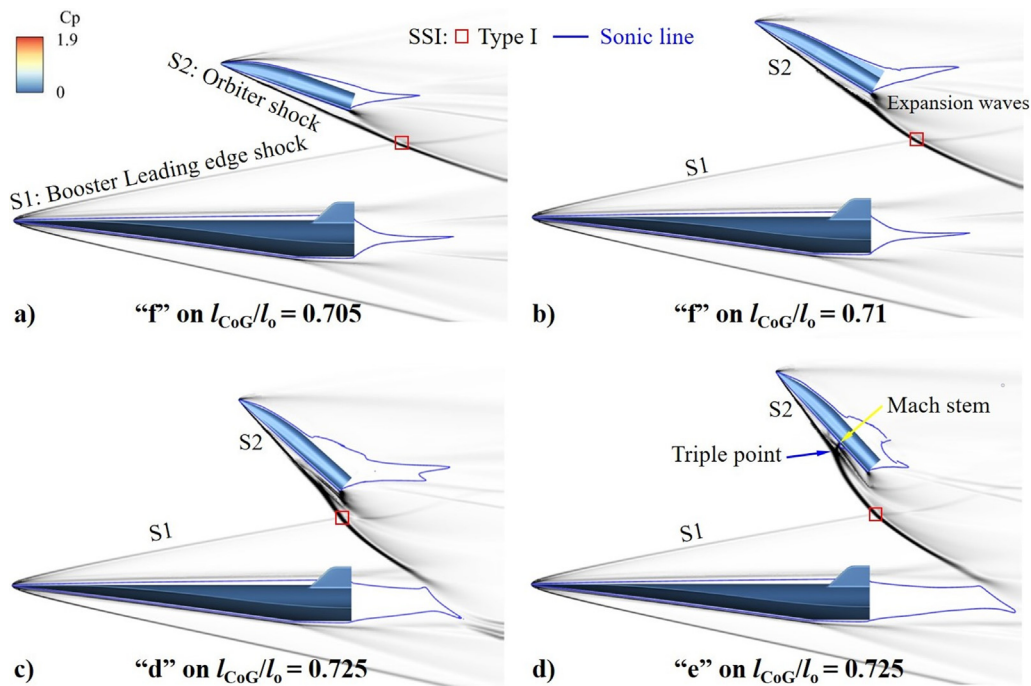
FIG. 22. Numerical schlieren and sonic line on the symmetry plane and wall pressure contour of several feature instantaneous flowfields of "d," "e," and "f" during stage separation.

shock structure under the orbiter, e.g., the compression waves covered by S2, as shown in Fig. 22(c), turn to the triple point and Mach stem, as shown in Fig. 22(d). The response pressure distributions are shown in Fig. 21(b), and with the high-pressure shifts upstream, the pitching moment in Fig. 19 increases from the minimum point "d" to "e."

In general, as the CoG shifts backward, the orbiter has the appropriate nose-up moment to resist or compensate for the nose-down moment contributed by the impingement of S2 on the afterbody of the orbiter. Therefore, the orbiter can break the interaction of the booster leading-edge shock and successfully separate from the booster with a positive pitching angle. In addition, the orbiter could not manifest invariant aerodynamic phenomena at the greater pitching angle after stage separation under conditions with larger l_{CoG}/l_o, as shown in Fig. 20.

3. Special unsafe stage separation of the two stages $(0.75 \leq l_{CoG}/l_o \leq 0.80)$

As shown in Fig. 12, the aerodynamic coefficients of both stages with $l_{CoG}/l_o = 0.75$ and 0.80 vary with huge fluctuation and different trends in contrast to these under the other conditions. Thus, distinct aerodynamic interactions occur during stage separation and have a significant effect. Figure 23 plots the time history of the pitching moment coefficients of the two stages when $l_{CoG}/l_o = 0.75$ and 0.80, and several feature points are labeled. The pitching moment coefficient of the booster under both conditions varies with similar trends, while that of the orbiter shows a huge difference between the two conditions.

Figures 24 and 25 show the typical flowfields of the feature instants marked in Fig. 23 to describe the flow characteristics that

account for the special aerodynamics during stage separation with $l_{CoG}/l_o = 0.75$. Apparently, the flow structures before instant "a" vary the same as those with $0.705 \leq l_{CoG}/l_o \leq 0.725$. However, the orbiter has a greater pitching moment as the CoG shifts backward further, resulting in a greater pitching angle and greater lift force and displacements, as shown in Figs. 9 and 12. At instant "a," the orbiter shock S2 incidents on the booster cause the SBLI and recirculation region. Due to the strong strength of S2, the shear layer S3 is lifted higher, and the separation shock S4 is induced. Moreover, shock waves S1 and S4 impinge on the points in front of the orbiter's CoG with high pressure so that its nose-up moment reaches the maximum. As the separation goes, as seen in Fig. 24(b), the reattachment shock S5 associated with high-pressure shifts downstream along the upper wall of the booster so that the nose-up moment of the booster reaches maximum, as shown in Fig. 26(b). In addition, the shear layer S3 is lifted higher and closer to the orbiter due to incident shock S2 with a greater shock angle. Moreover, the stronger SBLI induces the higher pressure downstream, and therefore, the greater adverse pressure gradient propagates upstream more forward in the subsonic zone, resulting in the lifting of the shear layer and forward moving separation shock S4. When the situation reaches instant "c," incident shock S2 has induced a larger separation, and the separated shear layer impinges on the afterbody of the orbiter. Moreover, shock waves S4 and S1 first intersect at the end point and then interact with S2 in type I, and the transmitted shock impinges on the middle part of the orbiter. Thus, the nose-up moment of the orbiter reaches the minimum, as shown in Fig. 23(a). Figures 25(a) and 25(b) show that the separated vortex develops and moves upstream in the subsonic zone under the increasing adverse pressure gradient caused by increasing strength incident shock S2, which impels
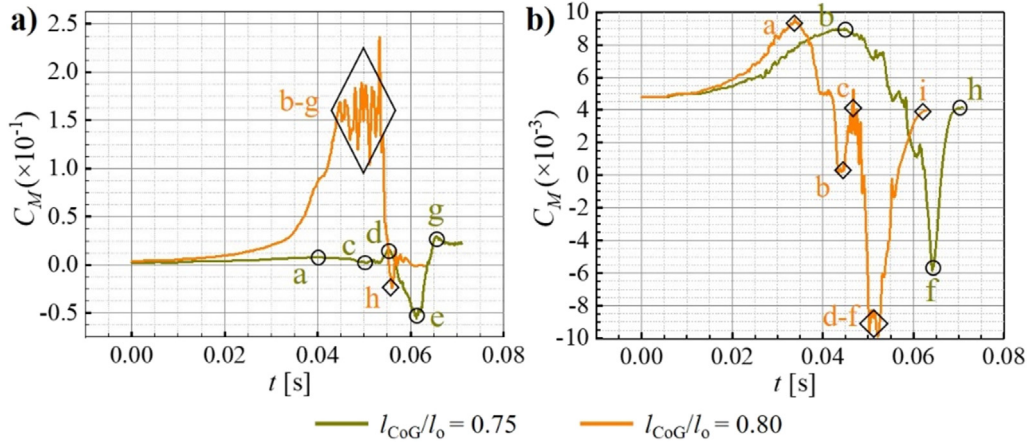
FIG. 23. Time history of the pitching moment coefficients of the two stages with $l_{CoG}/l_o = 0.75$ and 0.80 and corresponding feature points, circle points on the curve of $l_{CoG}/l_o = 0.75$, and diamond points on the curve of $l_{CoG}/l_o = 0.80$: (a) orbiter, (b) booster.
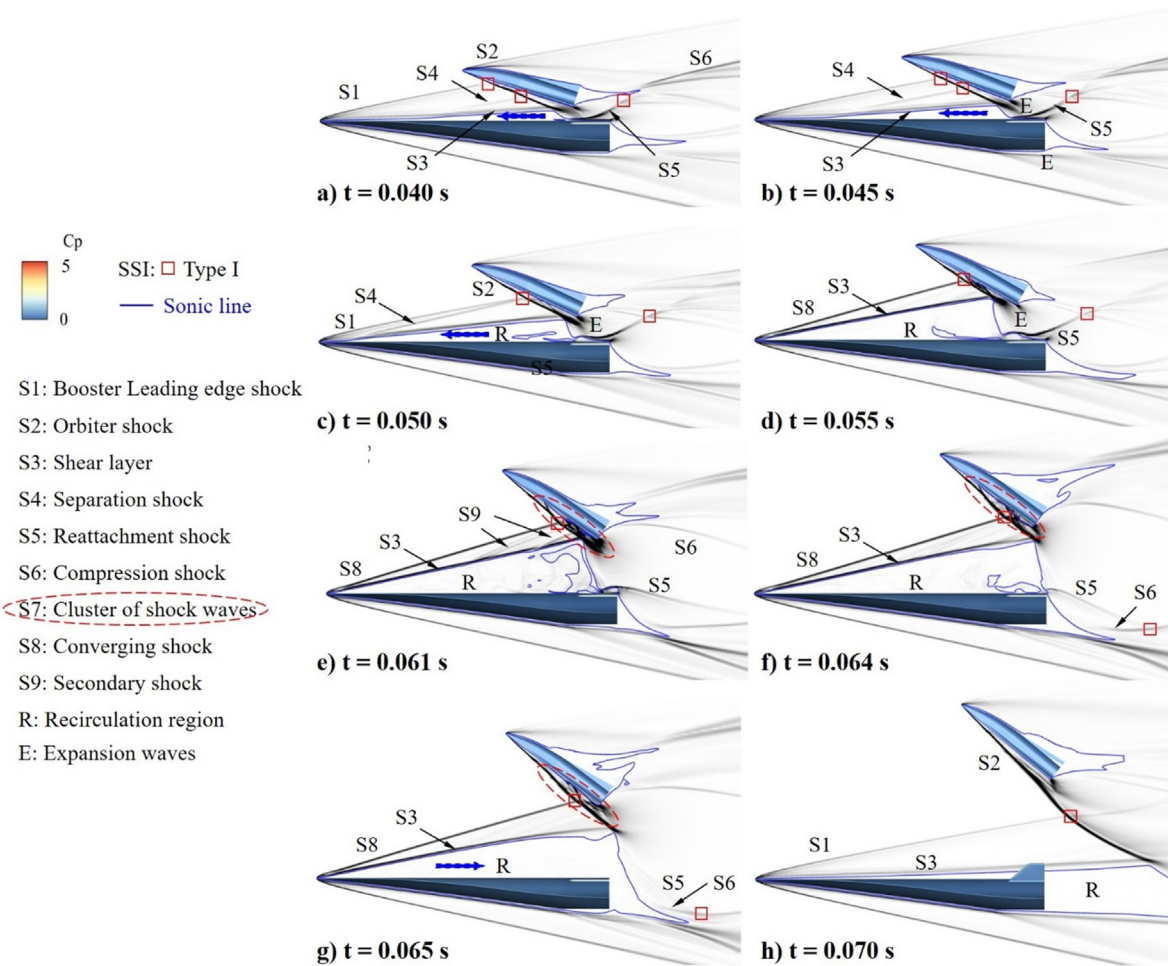
FIG. 24. Numerical schlieren and sonic line on the symmetry plane and wall pressure contour of several feature instantaneous flowfields during stage separation in the representative condition with $l_{CoG}/l_o = 0.75$.
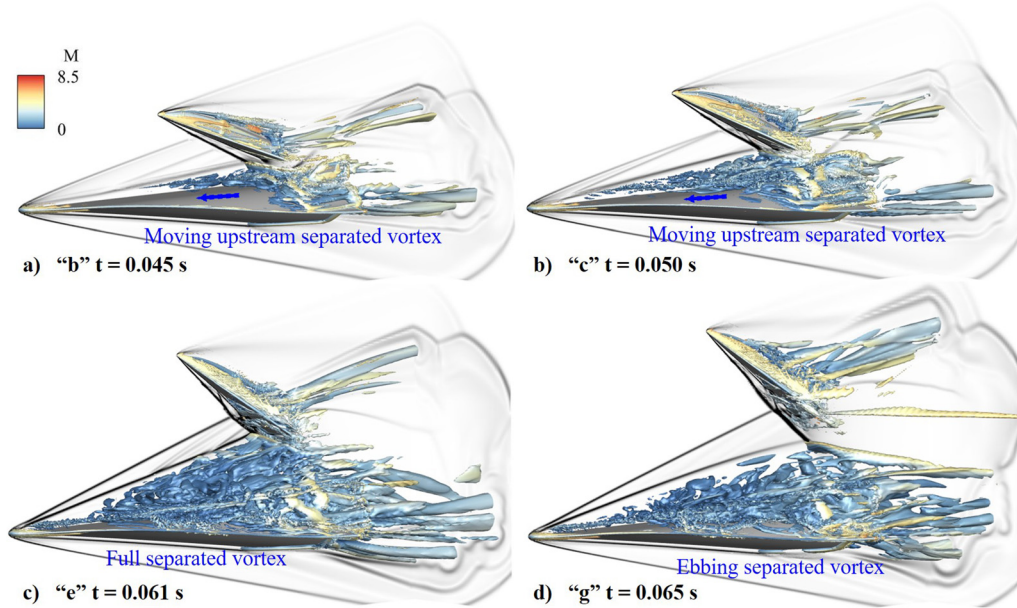
FIG. 25. Numerical schlieren on the symmetry plane and vortex structure illustrated by isosurface of Liutex magnitude of 8000 and colored by the Mach number of feature instantaneous flowfields during stage separation with $l_{CoG}/l_o = 0.75$.

the shear layer to be lifted increasingly higher and separation shock S4 to be stronger and moves upstream then pats on the booster leading edge shock S1. Therefore, shock waves S1 and S3 rendezvous and convert into a stronger converging shock S8 impinging on the orbiter at instant "d," causing the nose-up moment to reach the maximum, as shown in Fig. 23(a). The recirculation region extends to the booster leading edge. The larger recirculation region and subsonic zone are formed, and the orbiter is lifted higher with a greater pitching angle. The subsonic flow passes through the recirculation region and is expanded by expansion waves underneath the afterbody of the orbiter to the supersonic flow. Moreover, the part supersonic flow jets to the upper wall of the booster is decelerated by the ending shock, i.e., reattachment shock S5. In addition, the larger recirculation region on the booster will be maintained due to the high adverse pressure gradient

provided by the reattachment shock S5. The full and strong separated vortex is shown in Fig. 25(c), where the unsteady vortexes underneath the shear layer interact with each other and exchange kinetic energy, causing the shear layer to form some wrinkles resulting in secondary shock waves S9 origins on the shear layer. At instant "e," the shear layer and the converging shock impinge on the rearward of the orbiter and contribute to a great nose-down moment so that the pitching moment reaches the minimum. Due to the complex interactions between S8, the shear layer, and S2 near the orbiter, the cluster of shock waves accounting for the high pressure on the orbiter occurs, as shown in Fig. 24(e). As the orbiter separates to a higher position, where the shear layer no longer impinges on the orbiter and reattachment shock S5 shifts on the tail of the booster, the upper wall of the booster is covered by the recirculation region and separated vortex.
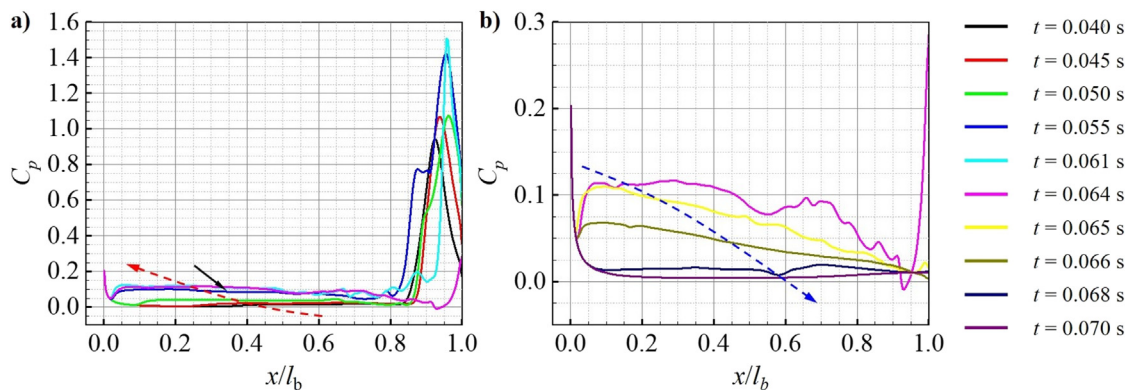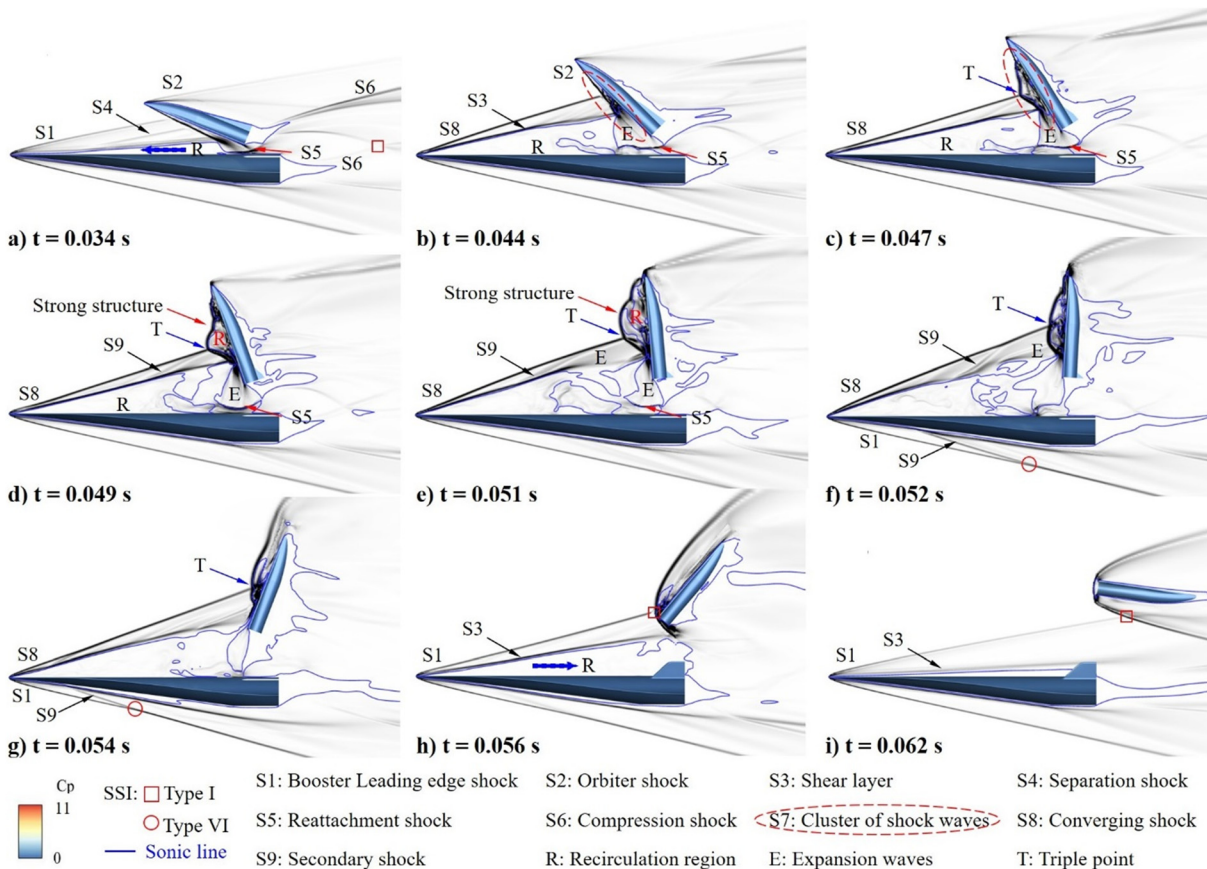

FIG. 26. Pressure coefficient along the upper symmetry line of the booster during stage separation with $l_{CoG}/l_o = 0.75$.

The high pressure on the rearward of the booster vanishes while still on the leading edge, so the nose-down moment of the booster reaches the maximum at instant "f." Due to the absence of the interaction of the shear layer on the orbiter and the strength of S7 being weaker, the pressure on the orbiter's afterbody decreases, and its pitching moment increases at instant "f" and reaches the maximum at instant "g." Due to the absence of the reattachment shock S5 on the booster and resulting high pressure, the adverse pressure gradient decreases to the positive gradient, and the separated vortex underneath the shear layer ebbs downstream and swarms into the wake, as shown in Figs. 24(g) and 25(d). The recirculation region diminishes, the shear layer returns to the booster, and the converging shock S8 degenerates into the leading edge shock S1. Additionally, the orbiter passes through just complex aerodynamic interaction and separates from the booster, and orbiter shock S2 intersects with S1 and then interacts with the developed shear layer in the wake, as shown in Fig. 24(h).

Figure 26 plots the pressure coefficient distributions along the upper wall of the booster at some instants during stage separation with $l_{CoG}/l_o = 0.75$. The pressure rise on the rearward at $0.8 \leq x/l_b \leq 1$ is attributed to the reattachment shock S5 shown in Figs. 24(a)–24(f). The pressure plateau represents the recirculation region on the booster, with the strength of S5 being stronger, the higher pressure on

the rearward. The higher adverse pressure gradient propagates upstream, and a larger recirculation region extends forward to the leading edge. Thus, the separated shear layer and the converging shock S8 are stronger, leading to a higher pressure plateau, as shown in Fig. 26(a). In addition, the separation point, i.e., the starting point of the plateau, also moves upstream and forward to the leading edge. When S5 vanishes and no longer exists on the booster anymore, the adverse pressure gradient converts to the positive pressure gradient due to the increasing pressure around the leading edge while decreasing pressure on the rearward, as shown in Fig. 26(b). Therefore, the recirculation region decreases, and the separated vortex moves downstream to wake. In addition, the shear layer reattaches on the booster so that the pressure distribution on the booster return to that at the isolated status. The "rise" and "descend" arrows in Fig. 26 indicate the pressure gradient behavior associated with the aerodynamic interaction and recirculation region shown in Figs. 24 and 25.

Figures 27 and 28 show the flow structures during stage separation with $l_{CoG}/l_o = 0.80$. The main flow structures, such as the separated shear layer S3, reattachment shock S5, the converging shock S8, and the moving recirculation region, are similar to those with $l_{CoG}/l_o = 0.75$. As the CoG shifts backward further, however, the orbiter shows faster pitching motion, and the booster full flow separation

FIG. 27. Numerical schlieren and sonic line on the symmetry plane and wall pressure contour of several feature instantaneous flowfields during stage separation in the representative condition with $l_{CoG}/l_o = 0.80$.

happens early. Consequently, the impinging of the S8 and shear layer on the orbiter promotes the pitching motion of the orbiter and induces a stronger structure around the orbiter, which substitutes the cluster of shock waves. Moreover, the recirculation region is formed on the orbiter, and the stronger structure is represented by the triple point structure shown in Figs. 27(c)–27(g). Since the flow separates on the orbiter, the unsteady vortex and variation of the strong structure are responsible for the fluctuations of the orbiter's aerodynamics, as shown in Fig. 23(a). Due to the high-pressure zone on its lower wall, the orbiter undergoes a pitching somersault under the greater nose-up moment, as shown in Fig. 27. As for the booster's pitching moment shown in Fig. 23(b), the nose-up moment maximizes because of the reattachment shock S5. With the compression effect of the S5 decreasing, the pressure on the rearward decreases. The pressure on the forebody of the booster increases with the strength increase in S8, as shown in Fig. 27(b), causing the nose-up moment to decrease to the minimum. However, the strength of S8 decreases at instant c, and the pressure on the forebody decreases, resulting in the nose-up moment increasing to the maximum, as shown in Fig. 23(b). In addition, the orbiter perpendicular to the booster during the somersault forms a strong downstream condition to enhance recirculation motion underneath the shear layer, causing the S8 to be stronger during instant "d"–"f" so that the nose-down moment reaches the maximum. The booster's pitching moment will recover as the recirculation region on the booster vanishes, and the shear layer attaches to the booster again, as shown in Fig. 27(i). On the other hand, due to the full separation on the booster, its leading-edge shock will be detached from the leading edge, thus losing "wave-ride" performance significantly. As a result, the pressure on the lower wall along the leading edge is no longer higher than that on the upper wall. Therefore, the forceful vortex downwashes along the leading edge, as shown in Fig. 28(c), and the side-flow momentum enters the boundary layer on the lower wall of the booster. Consequently, the shear layer is lifted slightly, and the secondary shock S9 underneath the booster is induced to interact with S1 with type VI, as shown in Figs. 27(f) and 27(g). The phenomena vanished as the separated vortex ebbed. The distinct flow phenomena occur when $l_{CoG}/l_o = 0.80$ instead of when $l_{CoG}/l_o = 0.75$ because of the downstream obstruction of the orbiter, which enhances the strength of the recirculation on the booster when $l_{CoG}/l_o = 0.80$. That is, the separated vortex in the recirculation region does not affect the lower wall of the booster and cross the leading edge, as shown in Fig. 25(c) with $l_{CoG}/l_o = 0.75$.

In general, as the CoG shifts backward further, the stage separation behavior of the orbiter is dominated by the rotation of the pitching, and the effect would be more notable as the l_{CoG}/l_o increases. Thus, the increasing orbiter pitching angle increases the strength of the orbiter shock S2 incidents to the boundary layer of the booster, causing the greater adverse pressure gradient to propagate upstream with a faster propagating speed. Therefore, the larger recirculation region induces a stronger converging shock and shear layer impinging on the orbiter, which, in turn, promotes the pitching speed of the orbiter. Thus, the positive feedback of the aerodynamic interaction associated with the pitching motion of the orbiter is formed, which induces the failure of stage separation. Furthermore, the effect of the feedback intensifies with the increase in the l_{CoG}/l_o. Figure 29 plots the functions of the shock angle against both pitching angular speed and angle to indicate the positive feedback. The orbiter's pitching angle could indicate the strength of the incident shock S2, and the angular speed could indicate its increasing rate. In the first phase, the shock angle represents the separation shock angle induced by the separated shear layer, as shown in Fig. 27(a). The shock angle increases with the pitching angle and angular speed, and vice versa. As the recirculation region extends upstream, the separation shock and the leading-edge shock converge to the converging shock, as shown in Fig. 27(b).

a) "a" t = 0.034 s — Moving upstream separated vortex
b) "d" t = 0.049 s — Full separated vortex
c) "f" t = 0.052 s — Vortex "downwash"
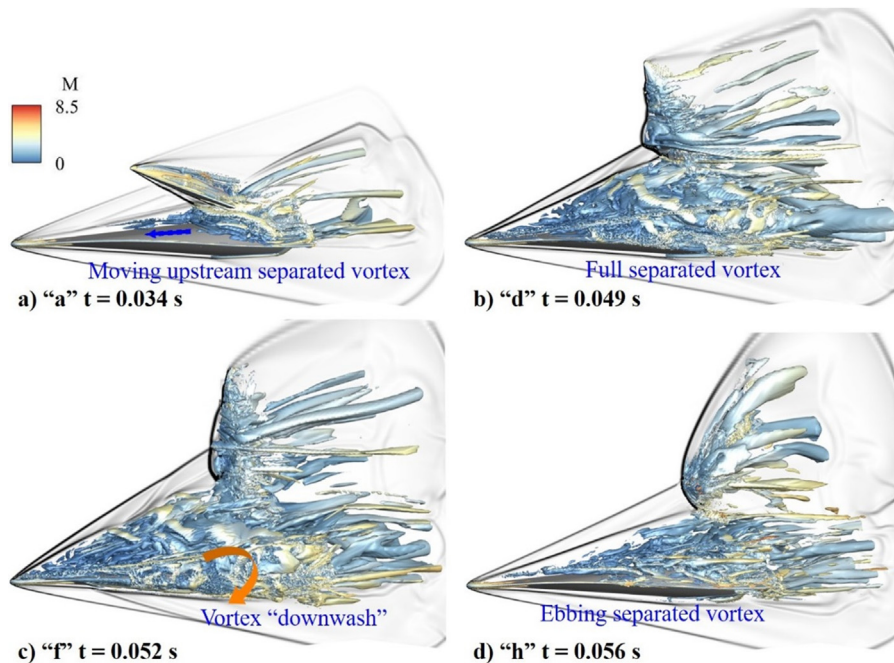d) "h" t = 0.056 s — Ebbing separated vortex

FIG. 28. Numerical schlieren on the symmetry plane and vortex structure illustrated by isosurface of Liutex magnitude of 8000 and colored by the Mach number of feature instantaneous flowfields during stage separation with $l_{CoG}/l_o = 0.80$.
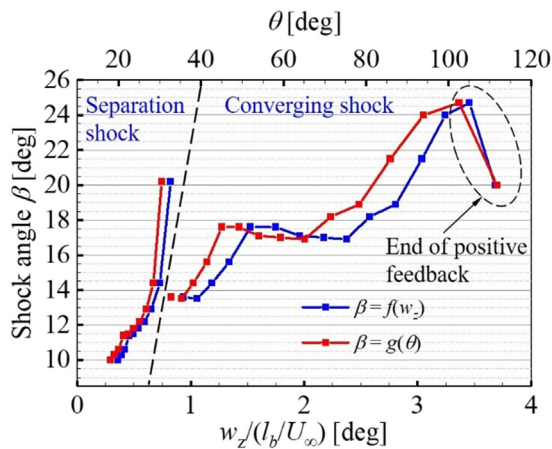
FIG. 29. The functions of the shock angle against both pitching angular speed and pitching angle during stage separation with $l_{CoG}/l_o = 0.80$.

The shock angle represents the converging shock angle in the second phase in Fig. 29. Also, the shock angle is increasing with the pitching angle and angular speed, and vice versa. Therefore, the shock angle indicates the strength of the recirculation region, aerodynamic interaction, and the pitching motion of the orbiter, which form positive feedback as analyzed. The positive feedback ends when the orbiter undergoes somersault so that the strong interaction downstream condition cannot be maintained. In addition, the TSTO stage separation with $0.75 \leq l_{CoG}/l_o \leq 0.80$ is unsafe because the orbiter may undergo somersault, and the booster would have a large recirculation region, causing its aerodynamics to fluctuate drastically, which should be avoided during stage separation.

V. CONCLUSIONS

This numerical study of how the orbiter's CoG affects the stage separation of TSTO vehicles at Mach 6.7 is performed to comparatively analyze the mechanism between the unsteady interaction and the aerodynamics of both stages and the resulting dynamic behavior in the different conditions with $0.65 \leq l_{CoG}/l_o \leq 0.80$. The results can be summarized as follows:

(1) The CoG significantly affects TSTO stage separation: the orbiter would nose-down to the booster, even resulting in the collision of the two stages with $0.65 \leq l_{CoG}/l_o \leq 0.70$; the orbiter successfully separates from the booster with $0.70 < l_{CoG}/l_o < 0.75$; and the orbiter performs pitching somersault, and large recirculation region appears on the booster if $0.75 \leq l_{CoG}/l_o \leq 0.80$.
(2) The trends of the aerodynamics and the flow structure during stage separation under the different conditions are almost the same during the early phase of separation. The flow is dominated by the SBLI, horseshoe vortex, and the type I and VI SSI. However, the large flow separation and strong aerodynamic interference resulted in strong structures such as triple point and cluster shock waves near the orbiter if $0.75 \leq l_{CoG}/l_o \leq 0.80$. The complex flow structure and the recirculation zone induced by the movement of the orbiter shock during stage separation are compared with those in the literature, which show good agreement.

(3) The orbiter collides with the booster due to the nose-down moment contributed by the SBLI near the rear of the orbiter when $0.65 \leq l_{CoG}/l_o < 0.70$, and the pitching moment switches from the nose-up moment to the nose-down moment when $l_{CoG}/l_o = 0.70$. However, the backward motion of the CoG endows the orbiter with an appropriate nose-up moment to resist or compensate for the nose-down moment if $0.70 < l_{CoG}/l_o < 0.75$. Furthermore, with the large backward motion of the CoG, the separation behavior of the orbiter is dominated by the rotation of the pitching if $0.75 \leq l_{CoG}/l_o \leq 0.80$, the positive feedback associated with the strong shock structure, the recirculation region, and the pitching motion induces the somersault of the orbiter and the full separation flow on the booster.

Overall, the hypersonic unsteady flow over the TSTO configuration during stage separation is demonstrated by presenting the flow-fields, the unsteady wall pressure along the stages, and the aerodynamic characteristics based on different CoG conditions. The CoG condition for stage separation in the current study is limited to 5% of the orbiter length, i.e., $0.70 < l_{CoG}/l_o < 0.75$. However, the other parameters besides the CoG, such as the initial interstage clearance and the AoA, which may also affect the stage separation performance, have not been investigated. In addition, the specific CoG conditions for different TSTO configurations may differ, although the key factors of the aerodynamic interference related to the stage separation results have been clarified. Therefore, the current discussions on how the CoG affects stage separation are a good start, and the remaining issues will be considered in future studies.

AUTHOR DECLARATIONS
Conflict of Interest

The authors have no conflicts to disclose.

Author Contributions

Yue Wang: Conceptualization (equal); Data curation (equal); Formal analysis (equal); Investigation (equal); Methodology (equal); Validation (equal); Visualization (equal); Writing – original draft (equal); Writing – review & editing (equal). **Yunpeng Wang:** Conceptualization (equal); Data curation (equal); Funding acquisition (lead); Methodology (equal); Project administration (equal); Resources (lead); Supervision (supporting); Writing – review & editing (equal). **Zonglin Jiang:** Funding acquisition (supporting); Project administration (supporting); Resources (supporting).

DATA AVAILABILITY

The data that support the findings of this study are available from the corresponding author upon reasonable request.

NOMENCLATURE

AoA	Angle of attack (deg)
C_D	Drag coefficient

C_L	Lift coefficient
C_M	Pitching moment coefficient
C_p	Pressure coefficient
D	Drag force (N)
d	Height of vehicle (m)
dt	Dimensional time step (s)
E, H	Total energy and total enthalpy per unit mass $(\mathrm{J \cdot kg^{-1}})$
$\boldsymbol{F_c}$	Convective fluxes
$\boldsymbol{F_v}$	Viscous fluxes
F_x, F_y, F_z	Force components exerted on body (N)
H	Enthalpy $(\mathrm{MJ \cdot kg^{-1}})$
h	Height of center or gravity or clearance (m)
I_{xx}	Moment of inertia about the x axis $(\mathrm{kg \cdot m^2})$
I_{yy}	Moment of inertia about the y axis $(\mathrm{kg \cdot m^2})$
I_{zz}	Moment of inertia about the z axis $(\mathrm{kg \cdot m^2})$
k_T	Coefficient of thermal conductivity $[\mathrm{W \cdot (m\ K)^{-1}}]$
L	Lift force (N)
L_s	Distance between the separation point and the end of the pressure plateau (m)
l	Length (m)
Ma	Mach number
M_x, M_y, M_z	Moment components exerted on body (N m)
M_z	Pitching moment (N m)
m	Mass (kg)
p	Pressure (Pa)
q	Dynamic pressure (Pa)
Re	Unit Reynolds number $(\mathrm{m^{-1}})$
Re_δ	Local Reynolds number based on the displacement of the boundary layer
T	Temperature (K)
t	Time (s)
U	Speed $(\mathrm{m \cdot s^{-1}})$
u, v, w	Velocity components in x, y, and z directions $(\mathrm{m \cdot s^{-1}})$
$\boldsymbol{V_g}$	Contravariant velocity vector at the surface of the control volume $(\mathrm{m \cdot s^{-1}})$
$\boldsymbol{V_r}$	Contravariant velocity vector relative to the motion of the grid $(\mathrm{m \cdot s^{-1}})$
V_x, V_y, V_z	Velocity components of body $(\mathrm{m \cdot s^{-1}})$
$\boldsymbol{W}$	Vectors of conservative variables
w	Span of vehicle (m)
x	Coordinate in the x direction (m)
y^+	Nondimensional wall spacing
β	Shock angle (deg)
$\Delta x, \Delta y, \Delta z$	Displacement in the x, y, and z direction (m)
Θ	Heat conduction $(\mathrm{W \cdot m^{-2}})$
θ	Pitching angle (deg)
μ	Coefficient of viscosity $(\mathrm{N \cdot s \cdot m^{-2}})$
ρ	Density $(\mathrm{kg \cdot m^{-3}})$
$\tau_{i,j}$	Component of viscous stress $(\mathrm{N \cdot m^{-2}})$
$\omega_x, \omega_y, \omega_z$	Angular velocity components of body $(\mathrm{rad \cdot s^{-1}})$

Subscripts

b	Booster
CoG	Center of gravity
CoP	Center of pressure
o	Orbiter
δ	Displacement thickness of the boundary layer (m)
0	Total condition
∞	Freestream condition

REFERENCES

[1] S. Weingertner, "SAENGER: The reference concept of the German hypersonics technology program," AIAA Paper No. 93-5161, 1993.

[2] U. Mehta and J. Bowles, "A two-stage-to-orbit spaceplane concept with growth potential," AIAA Paper No. 2001-1795, 2001.

[3] L. McKinney, D. Farrell, T. Bogar, and J. Stemler, "Investigation of TSTO propulsion system options," AIAA Paper No. 2006-8054, 2006.

[4] Y. P. Wang, H. Ozawa, H. Koyama, and Y. Nakamura, "Abort separation of launch escape system using aerodynamic interference," AIAA J. **51**, 270–275 (2013).

[5] S. J. Laurence, N. J. Parziale, and R. Deiterding, "Dynamical separation of spherical bodies in supersonic flow," J. Fluid Mech. **713**, 159–182 (2012).

[6] G. X. Xiang, C. Wang, H. H. Teng, and Z. L. Jiang, "Shock/shock interactions between bodies and wings," Chin. J. Aeronaut. **31**, 255–261 (2018).

[7] X. P. Xue, Y. Nishiyama, Y. Nakamura, K. Mori, Y. P. Wang, and C. Wen, "High-speed unsteady flows past two-body configurations," Chin. J. Aeronaut. **31**, 54–64 (2018).

[8] M. Patel and S. Navarro-Martinez, "Heat transfer to proximal cylinders in hypersonic flow," Phys. Fluids **35**, 036125 (2023).

[9] D. G. Wang, G. L. Han, M. K. Liu, and Z. L. Jiang, "Numerical investigation on unsteady interaction of oblique/bow shock during rotation based on non-inertial coordinate system," Phys. Fluids **34**, 121703 (2022).

[10] G. Kumar and A. De, "Modes of unsteadiness in shock wave and separation region interaction in hypersonic flow over a double wedge geometry," Phys. Fluids **33**, 076107 (2021).

[11] G. Kumar and A. De, "Role of corner flow separation in unsteady dynamics of hypersonic flow over a double wedge geometry," Phys. Fluids **33**(3), 036109 (2021).

[12] F. Lozano, J. Saavedra, and G. Paniagua, "Aero-thermal numerical characterization of blunt fin-induced shock wave–boundary layer interaction and its control through leading-edge cooling injection," Phys. Fluids **34**(9), 096110 (2022).

[13] J. H. Fan, J. A. Hao, and C. Y. Wen, "Nonlinear interactions of global instabilities in hypersonic laminar flow over a double cone," Phys. Fluids **34**(12), 126108 (2022).

[14] F. L. Tong, J. Lai, J. Y. Duan, S. W. Dong, X. X. Yuan, and X. L. Li, "Effect of interaction strength on recovery downstream of incident shock interactions," Phys. Fluids **34**(12), 125127 (2022).

[15] C. E. Sousa, R. Deiterding, and S. J. Laurence, "Dynamics of a spherical body shedding from a hypersonic ramp. I. Inviscid flow," J. Fluid Mech. **906**, A28 (2021).

[16] C. Butler, T. Whalen, C. Sousa, and S. J. Laurence, "Dynamics of a spherical body shedding from a hypersonic ramp. II. Viscous flow," J. Fluid Mech. **906**, A29 (2021).

[17] Y. Wang, Y. P. Wang, and Z. L. Jiang, "Numerical investigation of aerodynamic separation schemes for two-stage-to-orbit-like two-body system," Aerosp. Sci. Technol. **131**(Part A), 107995 (2022).

[18] Y. Wang, Y. P. Wang, C. Wang, and Z. L. Jiang, "Numerical study of the longitudinal stage separation for parallel-stage two-stage-to-orbit vehicle," Acta Aeronaut. Astronaut. Sin. **44**, 127634 (2023).

[19] Y. Wang, Y. P. Wang, C. Wang, and Z. L. Jiang, "Numerical investigation on longitudinal stage separation of spiked two-stage-to-orbit vehicle," J. Spacecr. Rockets **60**, 215–229 (2023).

[20] Y. Wang, Y. P. Wang, and Z. L. Jiang, "Experimental study of longitudinal stage separation of two-body configuration in shock tunnel," AIAA J. **60**, 6940–6946 (2022).

[21] Y. Wang, Y. P. Wang, and Z. L. Jiang, "Research on the test technology of longitudinal stage separation for TSTO in shock tunnel," Acta Aeronaut. Astronaut. Sin. **44**, 128126 (2023).

[22] J. P. Decker, "Aerodynamic interference effects caused by parallel-staged simple aerodynamic configurations at Mach numbers of 3 and 6," Report No. NASA-TN-D-5379 (NASA, 1969).

[23] J. P. Decker and A. Wilhite, "Technology and methodology of separating two similar size aerospace vehicles within the atmosphere," AIAA Paper No. 75-29, 1975.

[24] W. Schroder and G. Hartmann, "Analysis of inviscid and viscous hypersonic flows past a two-stage spacecraft," J. Spacecr. Rockets **30**, 8–13 (1993).

[25] T. Cvrlje, C. Breitsamter, and B. Laschka, "Numerical simulation of the lateral aerodynamics of an orbital stage at stage separation flow conditions," Aerosp. Sci. Technol. **4**, 157–171 (2000).

[26] W. Bordelon, A. Frost, and D. Reed, "Stage separation wind tunnel tests of a generic TSTO launch vehicle," AIAA Paper No. 2003-4227, 2003.

[27] K. Murphy, G. Erickson, and S. Goodliff, "Experimental stage separation tool development in Langley's unitary plan wind tunnel," AIAA Paper No. 2004-4727, 2004.

[28] H. Ozawa, K. Hanai, K. Kitamura, K. Mori, and Y. Nakamura, "Experimental investigation of shear-layer/body interactions in TSTO at hypersonic speeds," AIAA Paper No. 2008-723, 2008.

[29] H. Ozawa, K. Kitamura, K. Hanai, K. Mori, and Y. Nakamura, "Unsteady aerodynamic interaction between two bodies at hypersonic speed," Trans. Jpn. Soc. Aeronaut. Space Sci. **53**, 114–121 (2010).

[30] Y. Wang, Y. P. Wang, X. P. Xue, and Z. L. Jiang, "Numerical investigation on safe stage separation problem of a TSTO model at Mach 7," Chin. J. Theor. Appl. Mech. **54**, 526–542 (2022).

[31] J. Z. Lin, F. T. Xie, J. Zhong, D. Y. Zou, and Y. J. Pi, "Dual-body synchronous captive trajectory test technique in hypersonic wind tunnel," Acta Aerodyn. Sin. **40**, 1–10 (2022).

[32] S. Chakravarthy, "A unified-grid finite volume formulation for computational fluid dynamics," Int. J. Numer. Methods Fluids **31**, 309–323 (1999).

[33] H. Luo, J. Baum, and R. Lohner, "Extension of HLLC scheme for flows at all speeds," AIAA Paper No. 2003-3840, 2003.

[34] E. F. Toro, *Riemann Solvers and Numerical Methods for Fluid Dynamics: A Practical Introduction* (Springer Science & Business Media, New York, 2009).

[35] W. Sutherland, "The viscosity of gases and molecular force," London Edinburgh Dublin Philos. Mag. J. Sci. **36**, 507–531 (1893).

[36] J. R. Edwards, "An implicit multigrid algorithm for computing hypersonic, chemically reacting viscous flows," J. Comput. Phys. **123**, 84–95 (1996).

[37] H. Struchtrup, *Macroscopic Transport Equations for Rarefied Gas Flows: Approximation Methods in Kinetic Theory* (Springer Inc., Germany, 2005).

[38] Z. H. Wang, *Theoretical Modelling of Aeroheating on Sharpened Noses under Rarefied Gas Effects and Nonequilibrium Real Gas Effects*, Springer thesis (Springer, Beijing, 2014).

[39] Y. B. Gan, A. G. Xu, G. C. Zhang, Y. D. Zhang, and S. Succi, "Discrete Boltzmann trans-scale modeling of high-speed compressible flows," Phys. Rev. E **97**, 053312 (2018).

[40] M. K. Liu, G. L. Han, and Z. L. Jiang, "Experimental study on the evolution of mode waves in laminar boundary layer on a large-scale flat plate," Phys. Fluids **34**, 013612 (2022).

[41] K. Kitamura, T. Nakamura, I. Men'shov, and Y. Nakamura, "CFD analysis of aerodynamic interference between a delta wing and a hemisphere-cylinder," AIAA Paper No. 2004-1378, 2004.

[42] W. Schroeder and F. Mergler, "Investigation of the flowfield over parallel-arranged launch vehicles," AIAA Paper No. 93-3060, 1993.

[43] S. Tian, J. Fu, and J. Chen, "A numerical method for multi-body separation with collisions," Aerosp. Sci. Technol. **109**, 106426 (2021).

[44] M. S. Holden, M. MacLean, T. P. Wadhams, and A. Dufrene, "Measurements of real gas effects on regions of laminar shock wave/boundary layer interaction in hypervelocity flows for 'blind' code validation studies," AIAA Paper No. 2013-2837, 2013.

[45] R. Y. Mehrnaz and K. Doyle, "Assessment of CFD capability for hypersonic shock wave laminar boundary layer interactions," Aerospace **4**, 4020025 (2017).

[46] R. R. Heim, "CFD wing/pylon/finned store mutual interference wind tunnel experiment," Report No. AEDC-TSR-91-P4 (NASA, 1991).

[47] D. Snyder, E. Koutsavdis, and J. Anttonen, "Transonic store separation using unstructured CFD with dynamic meshing," AIAA Paper No. 2003-3919, 2003.

[48] C. Q. Liu, Y. S. Gao, S. L. Tian, and X. R. Dong, "Rortex—a new vortex vector definition and vorticity tensor and vector decompositions," Phys. Fluids **30**, 035103 (2018).

[49] Y. S. Gao and C. Q. Liu, "Rortex and comparison with eigenvalue-based vortex identification criteria," Phys. Fluids **30**, 085107 (2018).

[50] E. H. Hirschel and C. Weiland, *Selected Aerothermodynamic Design Problems of Hypersonic Flight Vehicles* (Springer Inc., Berlin, 2009).

[51] H. Babinsky and J. K. Harvey, *Shock Wave-Boundary-Layer Interactions* (Cambridge University Press, New York, 2011).